Cell Reports

Article

Role of VAMP7-Dependent Secretion of Reticulon 3 in Neurite Growth

Graphical Abstract

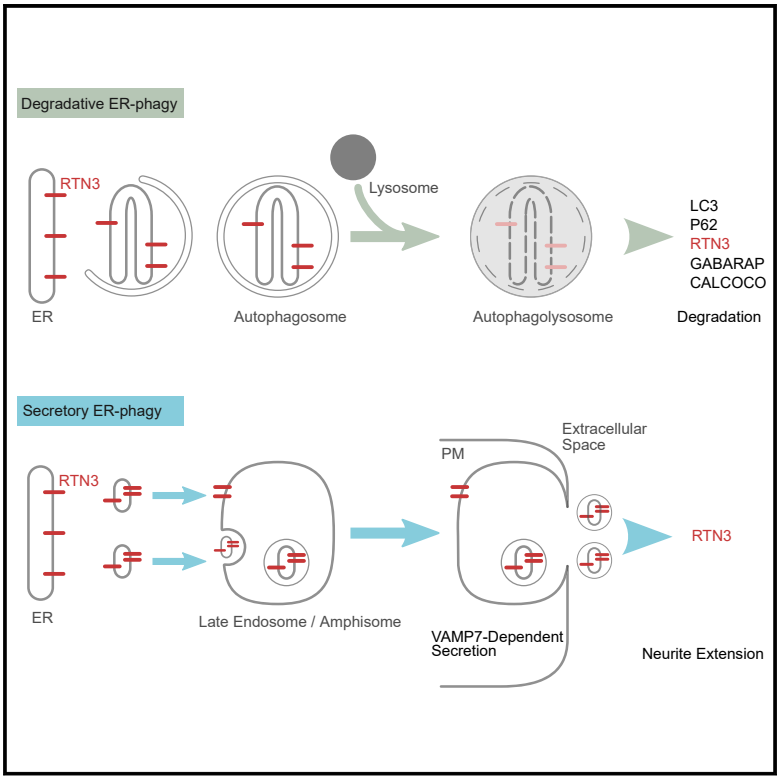

Highlights

- Nutrient restriction and autophagy regulate axonal growth and neuronal polarity
- VAMP7 mediates nutrient restriction/autophagy-dependent neurite growth
- VAMP7 mediates the secretion of ER-phagy factor Reticulon 3

Authors

José Wojnacki, Sébastien Nola, Philippe Bun, ..., Maria Isabel Colombo, Ida Chiara Guerrera, Thierry Galli

Correspondence

thierry.galli@inserm.fr

In Brief

VAMP7 is involved in exocytosis-mediated neurite growth and degradative autophagy. Using secretomics, Wojnacki et al. show that VAMP7 mediates the release of tubular ER-phagy receptor Reticulon 3, a secretory pathway greatly enhanced in autophagy-null neuronal cells. ER-phagy and unconventional secretion regulate neurite growth and polarization during nutrient deprivation.

Wojnacki et al., 2020, Cell Reports *33*, 108536
December 22, 2020
https://doi.org/10.1016/j.celrep.2020.108536

CellPress

Cell Reports

CellPress
OPEN ACCESS

Article

Role of VAMP7-Dependent Secretion of Reticulon 3 in Neurite Growth

José Wojnacki,[1,7] Sébastien Nola,[1] Philippe Bun,[2] Béatrice Cholley,[1] Francesca Filippini,[1] Mary T. Pressé,[1] Joanna Lipecka,[3] Sin Man Lam,[4] Julie N'guyen,[2] Axelle Simon,[1] Amine Ouslimani,[1] Guanghou Shui,[4] Claudio Marcelo Fader,[5] Maria Isabel Colombo,[5] Ida Chiara Guerrera,[3] and Thierry Galli[1,6,8,*]

[1]Université de Paris, Institute of Psychiatry and Neuroscience of Paris, INSERM U1266, Membrane Traffic in Healthy & Diseased Brain, 75014 Paris, France

[2]Université de Paris, NeurImag Imaging Facility, Institute of Psychiatry and Neuroscience of Paris, INSERM U1266, 75014 Paris, France

[3]University of Paris, Proteomics Platform Necker, Structure Fédérative de Recherche Necker, INSERM US24/CNRS UMS3633, 75015 Paris, France

[4]State Key Laboratory of Molecular Developmental Biology, Institute of Genetics and Developmental Biology, Chinese Academy of Sciences, 100101 Beijing, China

[5]Laboratorio de Biología Celular y Molecular, Instituto de Histología y Embriología, Universidad Nacional de Cuyo, CONICET, 5500 Mendoza, Argentina

[6]GHU PARIS Psychiatrie & Neurosciences, 75014 Paris, France

[7]Present address: Centre for Genomic Regulation, The Barcelona Institute of Science and Technology, 08003 Barcelona, Spain

[8]Lead Contact

*Correspondence: thierry.galli@inserm.fr

https://doi.org/10.1016/j.celrep.2020.108536

SUMMARY

VAMP7 is involved in autophagy and in exocytosis-mediated neurite growth, two yet unconnected cellular pathways. Here, we find that nutrient restriction and activation of autophagy stimulate axonal growth, while autophagy inhibition leads to loss of neuronal polarity. VAMP7 knockout (KO) neuronal cells show impaired neurite growth, whereas this process is increased in autophagy-null ATG5 KO cells. We find that endoplasmic reticulum (ER)-phagy-related LC3-interacting-region-containing proteins Atlastin 3 and Reticulon 3 (RTN3) are more abundant in autophagy-related protein ATG5 KO and less abundant in VAMP7 KO secretomes. Treatment of neuronal cells with ATG5 or VAMP7 KO conditioned medium does not recapitulate the effect of these KOs on neurite growth. A nanobody directed against VAMP7 inhibits axonal overgrowth induced by nutrient restriction. Furthermore, expression of the inhibitory Longin domain of VAMP7 impairs the subcellular localization of RTN3 in neurons. We propose that VAMP7-dependent secretion of RTN3 regulates neurite growth.

INTRODUCTION

Macroautophagy (henceforth referred to as autophagy) is an adaptive mechanism for the elimination of superfluous intracellular components and is upregulated in conditions of nutrient restriction. Autophagy is under the regulation of mammalian target of rapamycin complex 1 (mTORC1) and a signaling cascade of autophagy-related proteins (ATGs) (Boya et al., 2013; Mizushima et al., 2011). Nutrients and/or growth factor deprivation inhibits mTORC1 kinase activity on ULK1 (Ser757), a central kinase regulating the autophagic response. Non-phosphorylated ULK1 triggers the formation of the phagophore with membrane contributions from different donor compartments, effectively isolating cytoplasmic material for degradation. Upon autophagy stimulation, LC3 is cleaved and lipidated to form LC3-II, which binds to the phagophore, marking the biogenesis of the autophagosome, a double-membrane-limited organelle (Kim et al., 2011). This essential step depends on the multiprotein complex ATG5/12/16L1 (Matsushita et al., 2007). LC3-II recruits LC3-interacting-region (LIR)-containing proteins into the phagophore (Birgisdottir et al., 2013). The autophagosome can then fuse with (1) endosomes to form a so-called amphisome, (2) lysosomes to form an autolysosome, or even (3) the plasma membrane to deliver its content to the extracellular space (Klionsky et al., 2014; Ponpuak et al., 2015). These different routes require membrane fusion events; thus, they rely on vesicular (v)- and target (t)-SNARE proteins (Wang et al., 2016).

Interestingly, the v-SNARE VAMP7 with the t-SNAREs Syntaxin17 and SNAP29 or SNAP47 can mediate the fusion of membranes during the initial formation of the phagophore and also the fusion of mitochondrial-derived vesicles (MDVs) with endosomes (Aoyagi et al., 2018; Moreau et al., 2011; McLelland et al., 2016). VAMP7 mutants in the fly show autophagy defects in neurons (Takáts et al., 2013), and the VAMP7 knockout (KO) mouse shows mitophagy impairment in insulin-secreting pancreatic β cells (Aoyagi et al., 2018). Nevertheless, the role of v-SNAREs in autophagy is complex

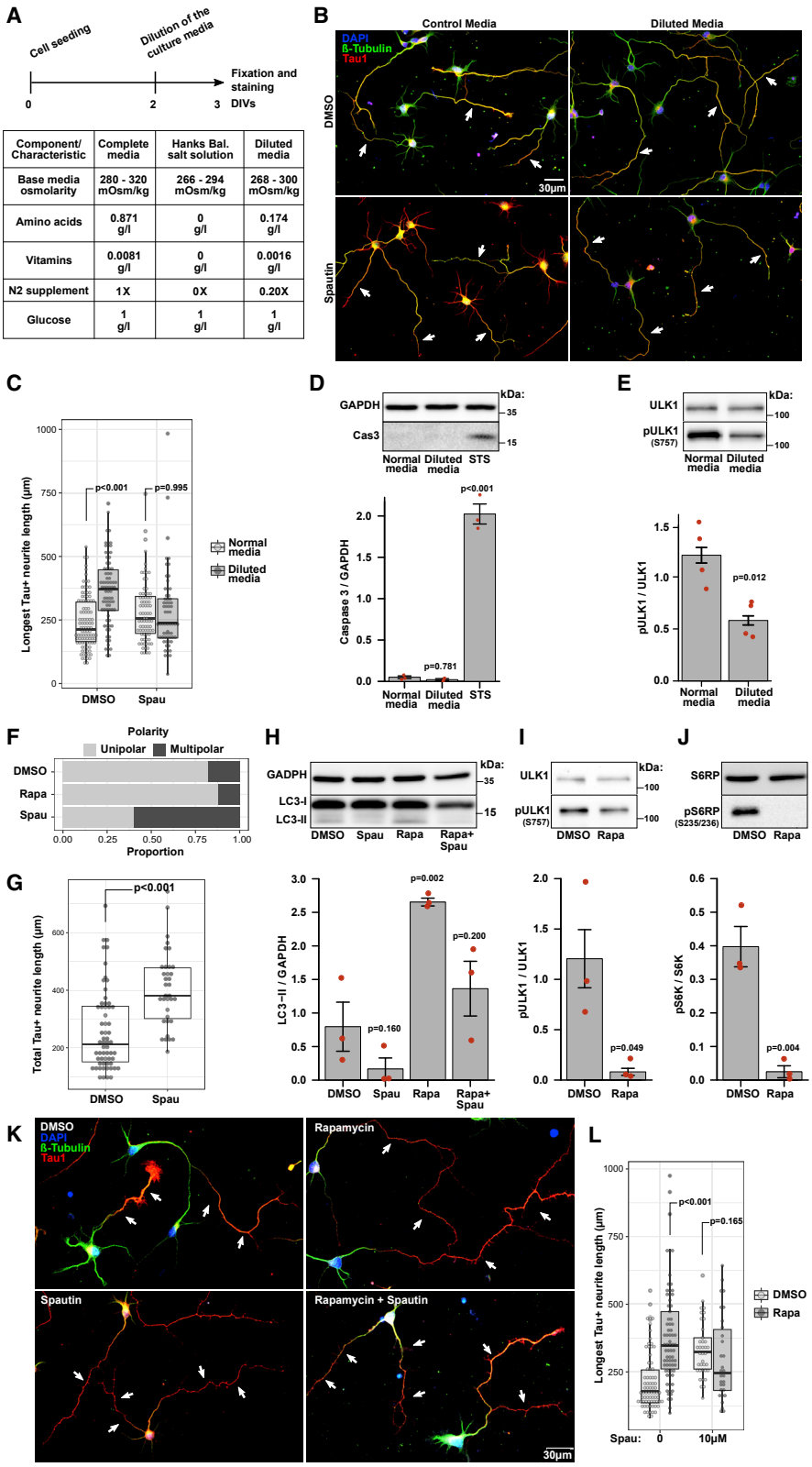

Component/ Characteristic	Complete media	Hanks Bal. salt solution	Diluted media
Base media osmolarity	280 - 320 mOsm/kg	266 - 294 mOsm/kg	268 - 300 mOsm/kg
Amino acids	0.871 g/l	0 g/l	0.174 g/l
Vitamins	0.0081 g/l	0 g/l	0.0016 g/l
N2 supplement	1X	0X	0.20X
Glucose	1 g/l	1 g/l	1 g/l

(legend on next page)

as evidenced by the overlapping functions of VAMP7, VAMP8, and Ykt6 in the fusion of autophagosomes with lysosomes (Itakura et al., 2012; Takáts et al., 2018). The potential function of VAMP7 in autophagic secretion has been suggested (Fader et al., 2012), but it has not yet been directly demonstrated. VAMP7 mediates lysosomal secretion as shown by the effect of its inhibitory Longin domain in epithelial cells (Proux-Gillardeaux et al., 2007) and silencing of its expression in astrocytes (Verderio et al., 2012). We and others have shown that VAMP7 plays an important role in the elongation of neurites during neuronal development, a cellular process that requires plasma membrane expansion. VAMP7 drives secretion during axonal growth by mediating membrane fusion with the t-SNAREs Syntaxin1 and SNAP25. It also regulates the transport and distribution of several cargo proteins including L1-CAM and the netrin receptor *Deleted in Colorectal Cancer* (DCC) (Alberts et al., 2003; Cotrufo et al., 2011; Winkle et al., 2014; Wojnacki and Galli, 2016). However, whether or how the roles of VAMP7 in autophagy and neurite growth are related has not been investigated.

To investigate whether the roles of VAMP7 in neurite growth and autophagy might be linked, we searched for the effect of nutrient restriction on axonal growth and hypothesized that VAMP7-dependent secretion could be involved. We found that beyond inducing autophagy, nutrient restriction stimulated axonal growth. Moreover, autophagy inhibition induced multipolar neurons. To precisely dissect the role of VAMP7 in this unexpected phenomenon, we took advantage of CRISPR-Cas9 genome editing to knock out VAMP7 in neuronal-like PC12 cells. To have autophagy-null cells to compare with, we also generated ATG5 KO PC12 cells. Using these cellular models, lipidomics, and proteomics of the secretome, we found that VAMP7 mediated the release of autophagy-related molecules LC3-II and LIR-containing endoplasmic reticulum (ER) proteins Reticulon 3 (RTN3). RTN3 has been shown to be involved in ER-phagy of tubular ER. This evidence thus supports the hypothesis that, during the course of neurite growth, VAMP7 mediates the secretion of molecules involved in ER-phagy.

RESULTS

Autophagy Modulates Axonal Growth

We tested the effect of several starvation conditions on axonal growth in neuronal cultures. Our aim was to mimic nutrient restriction while avoiding the extreme conditions that might result in rapid neuronal cell death as observed with complete glucose deprivation (Ramírez-Peinado et al., 2013). At 2 days *in vitro* (DIV), we diluted the N2 media five times with Hank's balanced salt solution (Figure 1A) to generate a condition where nutrients such as amino acids, vitamins, growth factors, and supplements were diluted, while salts and Glc remained unchanged. We found that this condition induced longer axons after 24 h, while it did not induce apoptosis as determined by the amount of cleaved caspase-3 (Figures 1B–1D). N2 culture media dilution induced autophagy in neurons as determined by detection of phosphorylated (p)Ser757-ULK1 levels (Figure 1E). A 48-h nutrient deprivation also induced longer axons (Figures S1A and S1B) but had an impact on neuronal viability as less neurons could be quantified. The effect of nutrient deprivation on axonal maximal length was attenuated by the specific autophagy inhibitor Spautin-1, which prevents the deubiquitinating activity of USP10 and USP13 (Liu et al., 2011) (Figures 1A and 1B), further demonstrating that axonal growth was dependent on functional autophagy. Moreover, autophagy inhibition with Spautin-1 affected neuronal polarity. Indeed, neurons treated with Spautin-1 still exhibited one axon longer than all other processes, but more neurons had multiple Tau1-positive neurites, with the presence of Tau1 being a mark of axonal specification (Bradke and Dotti, 2000) (Figures 1B, 1F, and 1K). The sum of the length of all Tau1-positive neurites was greatly increased upon Spautin-1 treatment (Figure 1G), suggesting that pre-existing minor processes turned into supernumerary axons as has been shown when GSK3β signaling is impaired (Witte et al., 2008; Yoshimura et al., 2005). The effect of nutrient deprivation on axonal length could not be reproduced by diluting only insulin (Figures S1C and S1D), unlike what was previously shown in the case of neuronal cell death (Young et al., 2009). To further establish

Figure 1. Effects of Nutrient Restriction and Autophagy Drugs on Growing Axons

(A) Scheme of the experimental design and table showing the concentration of the principal components of the normal and diluted culture media.

(B) Confocal images of hippocampal neurons (3 DIV) either unstarved or starved and treated with or without Spautin-1 (10 μM) for 24 h.

(C) Boxplot of the quantification of the length of longest Tau1-positive neurite in control and starved hippocampal neurons (Student's t test).

(D) Western blot of cleaved caspase-3 from neurons starved for 24 h. As a positive control of apoptosis, neurons were treated with staurosporine (100 nM) for 24 h. Bar plot showing the mean ± SEM amount of cleaved caspase-3 using glyceraldehyde 3-phosphate dehydrogenase (GAPDH) as a loading control. Each p value corresponds to the statistical ANOVA orthogonal contrast with the control condition.

(E) Western blot of the total and phosphorylated amount of ULK1 of 3 DIV cortical neurons either unstarved or starved for 24 h. Bar plot showing the mean ± SEM amount of pULK1 using total ULK1 as a loading control (Student's t test).

(F) Proportion of neurons with one (unipolar) or several (multipolar) Tau1-positive neurites in control neurons (DMSO treated), following treatment with rapamycin (Rapa; 50 nM) or Spautin-1 (10 μM).

(G) Boxplot of the quantification of the total length of all Tau1-positive neurites in control and Spautin-1-treated (10 μM) hippocampal neurons (Student's t test).

(H) LC3 and GAPDH blot of 3 DIV cortical neurons treated with Spautin-1 (10 μM), Rapa (50 nM), and a combination of both drugs for 24 h. Bar plot showing the mean ± SEM amount of LC3-II using GAPDH as a loading control (ANOVA orthogonal contrast).

(I and J) Blots of total and phosphorylated ULK1 and S6 ribosomal protein, respectively, of cortical neurons (3 DIV) treated with Rapa (50 nM) or without Rapa for 24 h. Bar plots show the mean ± SEM amount of pULK1 and pS6 ribosomal protein, respectively, using the non-phosphorylated proteins as loading controls (Student's t test).

(K) Images of cultured hippocampal neurons treated with or without Rapa (50 nM) and Spautin-1 (10 μM). Arrows indicate quantified Tau1-positive axons.

(L) Quantification of the total length of the longest Tau1-positive neurite in hippocampal neurons treated with Rapa (50 nM) and Spautin-1 (10 μM) (ANOVA orthogonal contrast).

Arrows indicate quantified Tau1-positive axons. Dots in boxplots represent the standardized individual values of all experimental replicates.

the role of autophagy in axonal growth, we treated hippocampal neurons with the autophagy inducer rapamycin (50 nM) for 24 h (Figures 1H–1L and S1E). The detection of LC3-II, pSer757-ULK1 and pSer235/236-S6 ribosomal protein levels by western blotting confirmed autophagy activation in neurons upon rapamycin treatment (Figures 1H–1J), and this was coincident with enhanced axonal growth (Figures 1K, 1L, and S1E). In addition, 200 nM resveratrol and 75 nM Torin1 showed similar effects (Figures S1F–S1I). The effects of rapamycin and Torin1 in axonal extension were reversed by Spautin-1 (Figures 1K, 1L, S1H, and S1I), further demonstrating that the increased maximal axonal growth was triggered by an autophagy-dependent process.

Polarization of Autophagy-Related Proteins and VAMP7 in Developing Neurons

We then hypothesized that neuronal polarization might be associated with the recruitment of ATG proteins in the growing axon. To test this hypothesis, we cultured rat hippocampal neurons and characterized the distribution of LC3 during stages 2–3 when axonal growth is at its peak (Dotti et al., 1988). We expressed GFP to obtain a measurement of the cell volume and stained neurons for endogenous LC3. We quantified the density of LC3 staining as the ratio of LC3 and GFP signals. We found a striking concentration of LC3 in the axon when neurons transition from stage 2 to stage 3 and during late stage 3, indicating the association of axon specification with the autophagic machinery (Figures 2A–2E). In addition, there was a positive correlation between the length of the axon and the density of LC3 (Figure 2F). If LC3 polarizing to the axon corresponds at least in part to VAMP7-positive secretory vesicles then we would expect that autophagy should increase the amount of VAMP7, LC3, and the secretory vesicle tether exocyst in axonal tips (EauClaire and Guo, 2003). Indeed, the exocyst subunit Sec6 marks secretory vesicles involved in neurite growth (Vega and Hsu, 2001). We thus treated neurons with rapamycin for 4 h to effectively induce autophagy as detected by the appearance of LC3-II by western blotting (Figures S2A and S2B). This treatment doubled the amount of VAMP7-, LC3-, and Sec6-positive spots in axonal growth cones compared with untreated neurons (Figures 2G, 2H, 2J, 2L, and 2N), while growth cone area remained unaffected (Figure 2M). Co-localization between LC3 and Sec6 was unaffected by rapamycin (Figures 2I and 2K), suggesting that autophagy induced a general increase in the amount of these vesicles in growth cones. Interestingly, growth cone concentration of SNAP29, a t-SNARE that pairs with VAMP7 and inhibits its secretory activity (Kuster et al., 2015) as well as mediates autophagosome-lysosome fusion (Guo et al., 2014), was not significantly affected by rapamycin as determined by immunostaining in the axonal growth cone (Figures S2E and S2F) or the total amount of protein detected by western blotting (Figure S2G). Additionally, we also tested O-linked β-*N*-acetylglucosamine (O-GlcNAc) modification of SNAP29 as this is associated with fusion between autophagosomes and lysosomes and with autophagic flux (Guo et al., 2014). No significant O-GlcNAcylation of SNAP29, VAMP7, or Sec6 was observed under our experimental conditions (Figures S2H–S2K). These results strongly suggest that a pool of Sec6/LC3/VAMP7-positive vesicles can concentrate in growing axons, particularly in growth cones, but these vesicles appear unrelated to autophagosome-lysosome fusion.

We then studied the *in vivo* dynamics of VAMP7 in neurons. We imaged both ATG9a, which is an autophagy-related membrane protein involved in autophagosome biogenesis, and VAMP7 because previous study found that these proteins co-localized (Aoyagi et al., 2018). ATG9a is localized in part to late endosomes in neurons (Tamura et al., 2010). We found the occurrence of ATG9a-red fluorescent protein (RFP)/GFP-VAMP7-positive punctae moving both anterogradely and retrogradely in the axons of 3 DIV hippocampal neurons (Figure S3A; Video S1). We also found that mCherry-LC3B and GFP-VAMP7 co-localized in anterogradely and retrogradely moving particles in growing axons (Figure S3B; Video S2). Co-localization between LC3 and VAMP7 was high and not modified by rapamycin (Figures S3B–S3D). However, net vesicular displacement and particle size were significantly increased upon rapamycin addition (Figures S3B, S3E, and S3F). The average speed of both retrogradely and anterogradely moving punctae was equally increased after rapamycin treatment (Figure S3G). These results led us to hypothesize a potential involvement of VAMP7 in a secretory mechanism that would be recruited upon autophagy induction in neurites.

VAMP7 Mediates NGF- and Autophagy-Induced Neurite Growth

To decipher the molecular mechanism linking autophagy, secretion, and neurite growth in greater detail, we generated VAMP7 and ATG5 KO PC12 cells by using CRISPR-Cas9 genome editing (Figures S4A–S4D) and compared the behavior of wild-type (WT), VAMP7 KO, and ATG5 KO PC12 cells in several assays. We chose PC12 cells because neurite growth induced by nerve growth factor (NGF) was previously shown to depend on VAMP7 (Martinez-Arca et al., 2000; Racchetti et al., 2010). First, we treated WT, VAMP7, and ATG5 KO cells with NGF to trigger neurite growth (Greene and Tischler, 1976). VAMP7 KO cells showed a strong decrease in neurite growth (as measured by the longest process), while it was increased in ATG5 KO cells compared with WT (Figures 3A and 3B). We then treated the cells with rapamycin and observed that the length of the single longest neurite was increased in WT and ATG5 KO, but not in VAMP7 KO, cells (Figures 3A and 3B). When we included the longest process and its branches, neurite growth in ATG5 KO cells was increased and showed more ramifications compared with WT (Figures 3A and 3C). Rapamycin had no additional effect on total neurite length (primary neurites plus branches) in any of the three cell types (Figures 3A and 3C). These results suggest that ATG5 KO cells resulted in longer and more branched neurites, a result in agreement with the effect on Spautin-1 inducing multipolar neurons described above (Figure 1). VAMP7 KO cells were strongly impaired for neurite growth and insensitive to rapamycin (Figures 3A–3C). Re-expression of GFP-VAMP7 fully rescued both NGF-dependent and rapamycin-induced neurite growth (Figures 3D and 3E).

Lipidomics and Secretomics of VAMP7 and ATG5 KO

To gain insight into how ATG5 and VAMP7 might regulate neurite growth, we carried out lipidomics and proteomics in our

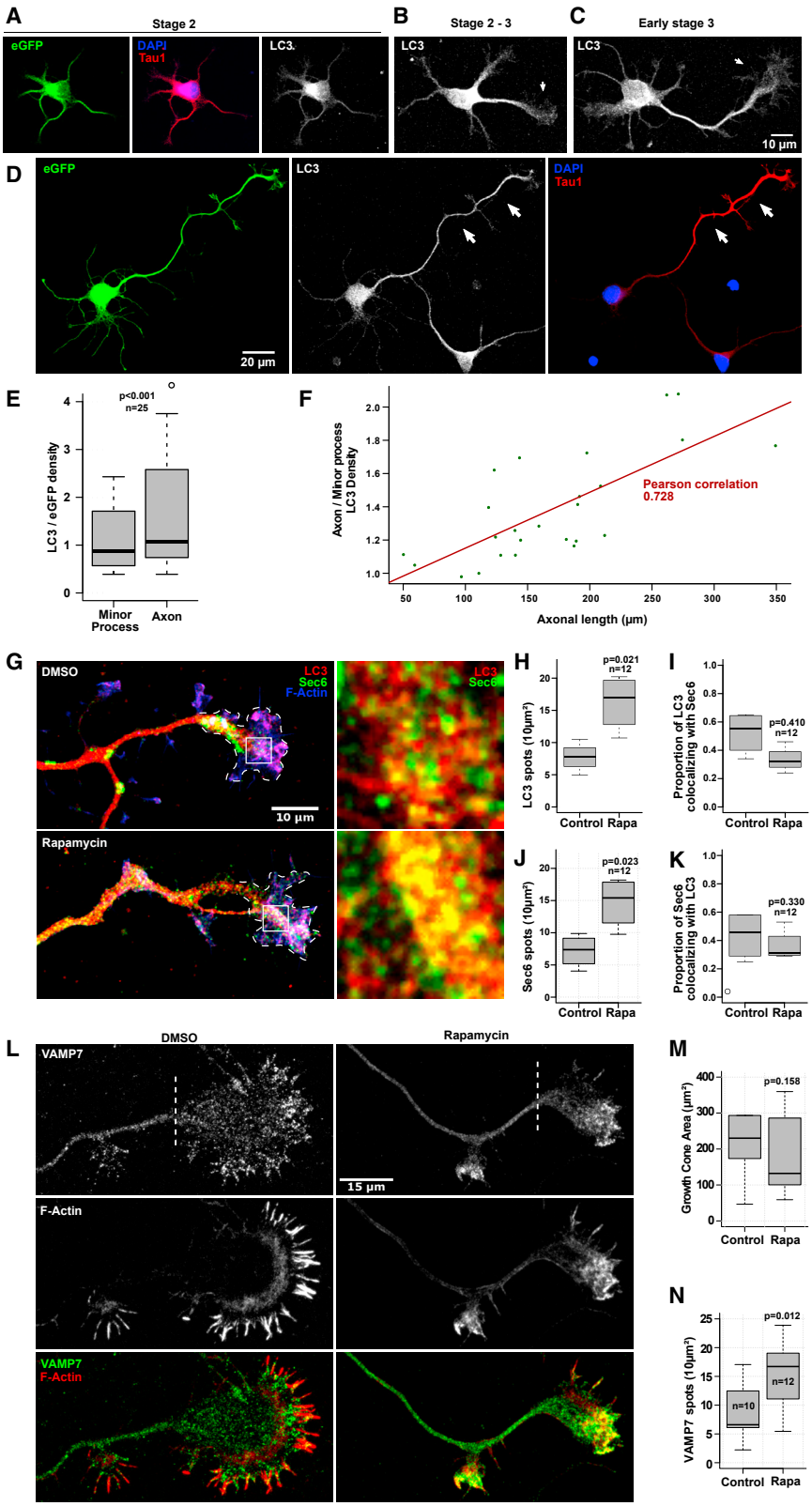

Figure 2. LC3 Is Polarized to the Fast-Growing Axon in Developing Neurons and Co-localizes with the Exocyst in Growth Cones

(A–D) Images showing the distribution of endogenous LC3 in GFP-expressing developing hippocampal neurons. Non-polarized neuron (A), stage 2–3 transition (B), early stage 3 (C), and late stage 3 (D). For (A)–(C), images share the same scale bar as in (C).

(E) Boxplot showing the amount of LC3 in minor processes and axons. GFP was used as a control for the differential volume of the neuronal processes (paired Student's t test).

(F) Plot showing the correlation between axonal length and LC3 density compared with the minor processes. Green dots are the individual observations.

(G) Images showing endogenous Sec6 and LC3 in the axonal growth cones of polarized (3 DIV) hippocampal neurons treated with or without Rapa (50 nM) for 4 h. High-magnification images of selected areas of the axonal growth cones (white boxes) are displayed in right panels.

(H and J) Boxplots showing the quantification of the number of Sec6- and LC3-positive spots in the axonal growth cone (the growth cone is delimited by the white dashed lines in G) (Student's t test).

(I and K) Boxplots showing the quantification of the proportion of LC3 spots that co-localize with Sec6 and the proportion of Sec6 spots that co-localize with LC3, respectively, and treated with Rapa (50 nM) or without Rapa for 4 h (Student's t test).

(L) Images of polarized hippocampal neurons (3 DIV) stained for endogenous VAMP7 and treated with Rapa (50 nM) or without Rapa for 4 h. The F-actin staining was used to define the growth cone, and the dashed line marks the beginning point for what we considered the growth cone during quantification.

(M and N) Boxplots showing the quantification of the growth cone area and the number of VAMP7 spots, respectively (Student's t test).

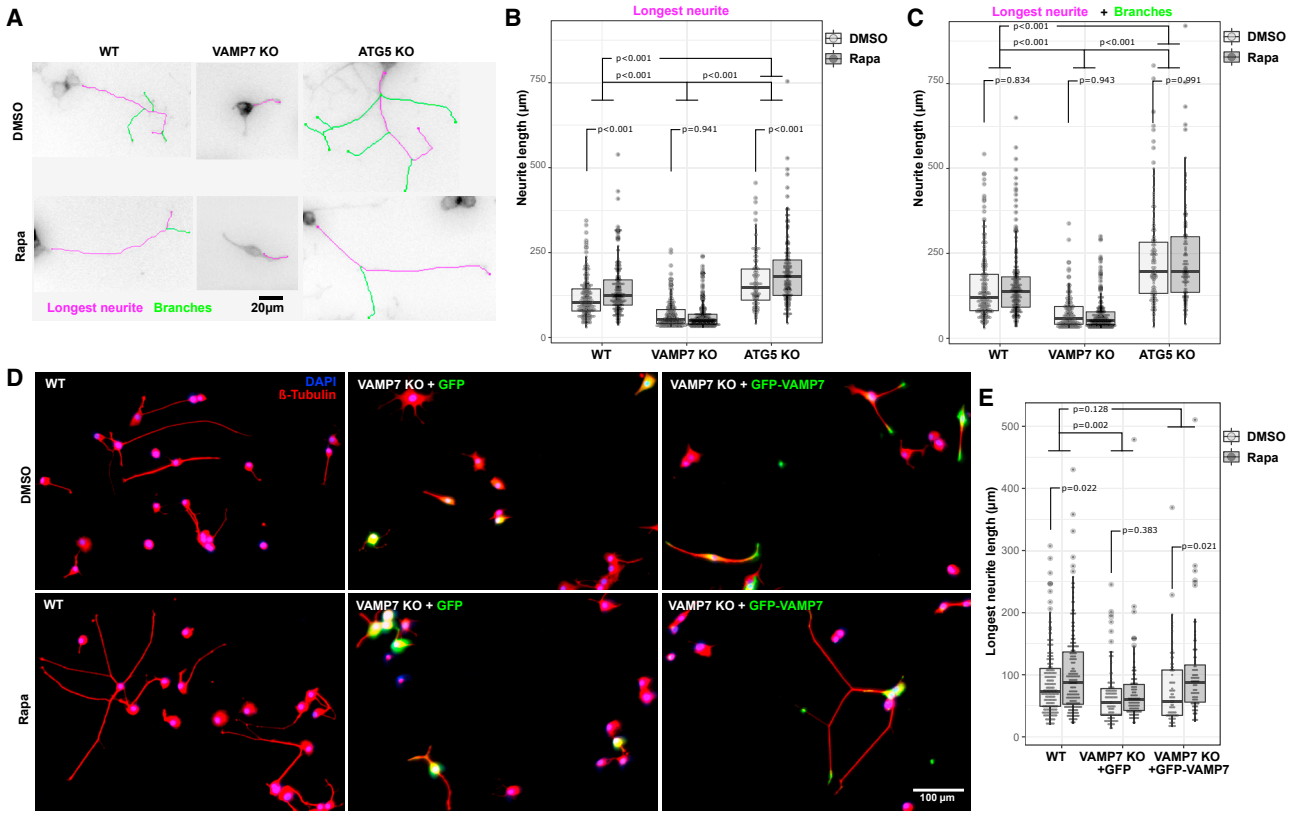

Figure 3. Effect of VAMP7 and ATG5 KO on Neurite Growth in NGF-Differentiated PC12 Cells

(A) Widefield images (negative display) of tubulin-labeled WT, VAMP7 KO, and ATG5 KO PC12 cells differentiated with NGF (50 ng/mL) for 1 week and then left untreated or treated with Rapa (100 nM) overnight. Pink and green line indicates the single longest process and the connected branches, respectively.

(B) Boxplot of the length of the longest neurite (pink line in A) for each condition shown in (A).

(C) Boxplot of the length of the longest process and branches (pink and green lines in A) for each condition shown in A. The p values correspond to the statistical ANOVA test for each genotype and Tukey statistical test for each experimental condition.

(D) Images of non-transfected WT, VAMP7 KO cells transfected with GFP, and VAMP KO PC12 cells transfected with GFP-VAMP7, treated with NGF (50 ng/mL) for 1 week and then treated with Rapa (100 nM) or without Rapa for 24 h.

(E) Boxplot showing the length of the single longest neurite in PC12 cells shown in (D). Each p value corresponds to an ANOVA test between the two conditions. The p values on top of the plot show the differences among the genotypes after an ANOVA test.

PC12 cell lines following NGF differentiation. Lipidomic analysis of WT, VAMP7 KO, and ATG5 KO PC12 cells showed that specific lipids involved in neurite extension were altered in each of the mutants relative to WT (Figures 4A and 4B). In ATG5 KO cells, enhanced levels of several glucosylceramides (GluCers) including GluCer d18:0/16:0 and GluCer d18:1/18:0 were observed. The increased levels of GluCers and enhanced neurite growth in ATG5 KO compared with WT PC12 cells in our study were in accordance with a previous report on the inhibitory effects of GluCer synthase inhibitor on neurite outgrowth in PC12 cells (Mutoh et al., 1998). In particular, impeding GluCer biosynthesis was found to inhibit neuronal sprouting, which was attributed to the depletion of downstream complex glycosphingolipids such as gangliosides in PC12 cells (Mutoh et al., 1998). Several sphingomyelins (SMs) were reduced in ATG5 KO cells (Figure 4A), suggesting that the enhanced levels of GluCers may be partly attributed to elevated breakdown of SMs. Importantly, accumulation of ceramides has been previously found in *Arabidopsis* upon ATG5 inactivation (Havé et al., 2019); therefore, it is likely a conserved mechanism. On the other hand, VAMP7 KO cells exhibited reduced levels of phosphatidylethanolamines (PEs) such as PE 38:4 and PE 34:2 and elevated plasmalogen phosphatidylcholines compared with WT (Figure 4B). Previous work had shown that the ethanolamine moiety of PE derived from phosphatidylserine is actively re-acylated only in PC12 cells undergoing NGF-induced neuritogenesis (Ikemoto and Okuyama, 2000). This result is particularly interesting because LC3 and other ATG8 molecules bind PE (Kabeya et al., 2004; Thukral et al., 2015). This further suggests that maintaining the intracellular pools of PEs may be important for both LC3 recruitment to membranes and NGF-induced neuritogenesis in PC12 cells.

We then conducted a proteomic analysis of the cell lysate and secretome of WT, ATG5, and VAMP7 KO PC12 cells. To avoid false positive results and remove extracellular vesicles (EVs) present in the cell culture media, we cultured cells without serum for 20 h before collecting the culture medium. Independent biological and technical triplicate experiments were

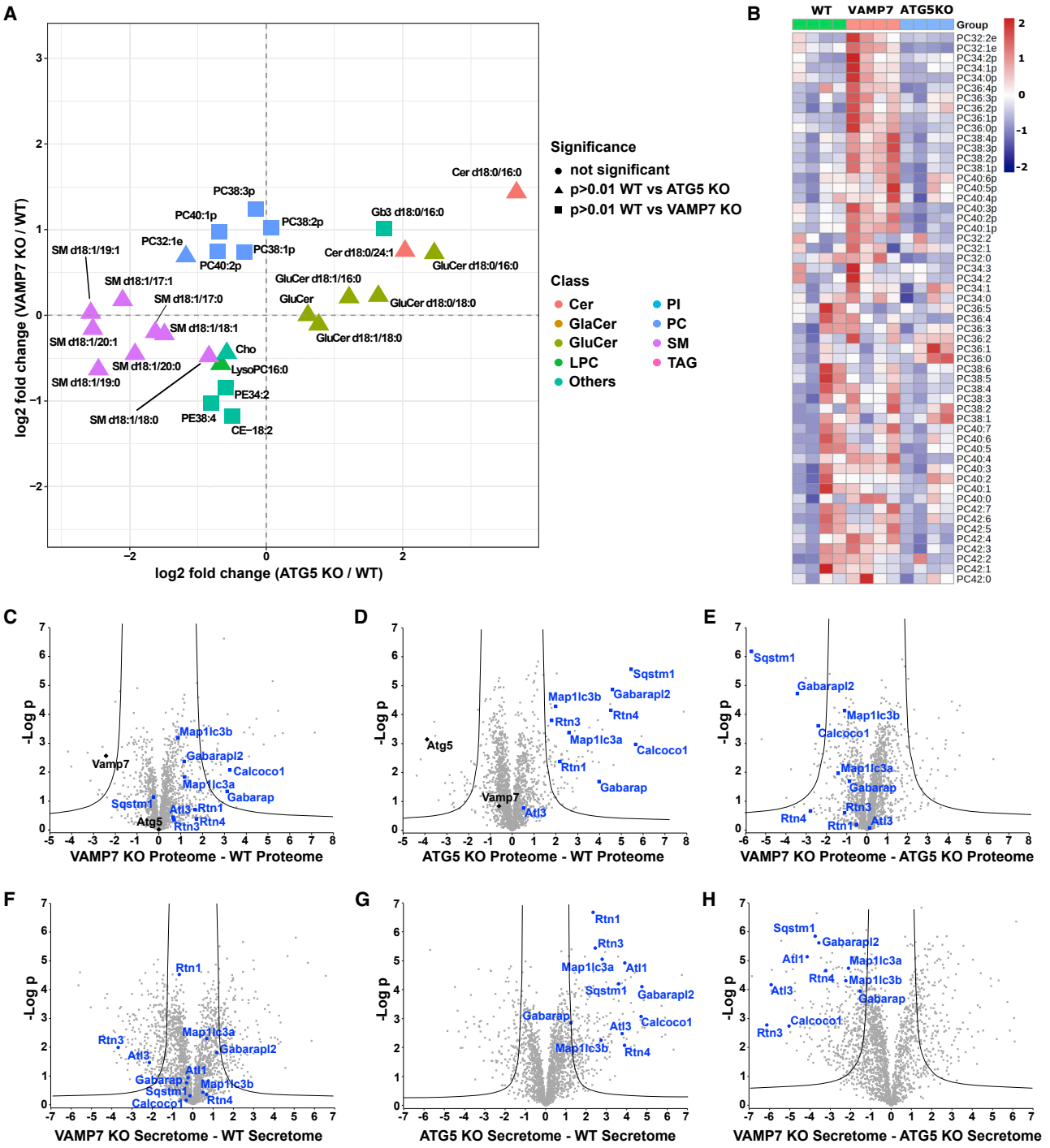

Figure 4. Lipidomic and Secretomic Analysis of WT, VAMP7 KO, and ATG5 KO PC12 Cells

(A) Scatterplot of the changes in cellular lipid profiles in VAMP7 KO (vertical axis) and ATG5 KO (horizontal axis) relative to WT PC12 cells. Lipids that were significantly altered ($p < 0.05$ from Student's t test) were enlarged and are represented by rectangles (VAMP7 KO versus WT) and triangles (ATG5 KO versus WT).

(B) Heatmap plot showing the difference in abundance of plasmalogen (PCs) lipid species in WT, VAMP7 KO, and ATG5 KO PC12 cells.

(C–E) Volcano plots showing the proteome of the extracted proteins significantly enriched in WT versus VAMP7 KO (C), WT versus ATG5 KO (D), and ATG5 KO versus VAMP7 KO (E). Black lines denote the statistical significance boundary. Proteins of interest are highlighted in blue.

(F–H) Volcano plots showing the secretome proteins significantly enriched in WT versus VAMP7 KO (F), WT versus ATG5 KO (G), and ATG5 KO versus VAMP7 KO (H). Black lines denote the statistical significance boundary. Proteins of interest are highlighted in blue.

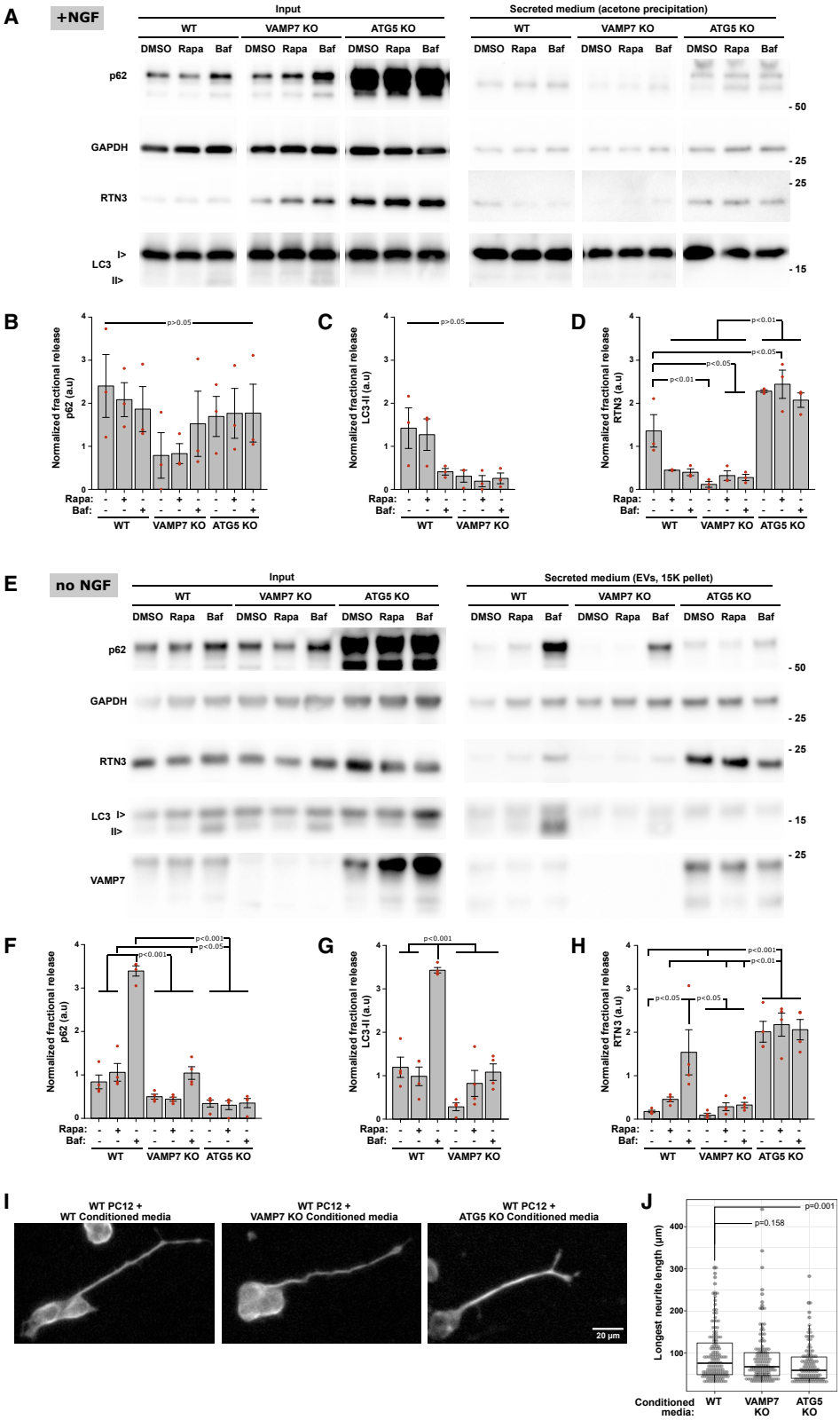

(legend on next page)

analyzed by mass spectrometry so that a quantitative analysis could be performed both in cell lysates and secretomes. Compared with WT samples, ATG5 and VAMP7 were undetectable in their respective KO PC12 cell line (Table S2). These data confirmed the genotypes of our cell lines and the sensitivity and reliability of our approach. We then analyzed the secretome of WT, VAMP7 KO, and ATG5 KO PC12 cells. We found that WT cells released proteins that were significantly less abundant in the VAMP7 KO secretome (Figures 4F; Table S2, secretome: filter "DOWN V7"). In the secretome of ATG5 KO cells, we found several autophagy-related proteins that were significantly increased (RTN1, CALCOCO1, Atlastin/ATL1, SQSTM1/p62, MAP1LC3B/LC3b, RTN4, MAP1LC3A/LC3a, GABARAP, GABARAPL2, RTN3, ATL3; Figure 4G; Table S2, secretome: filter "UP ATG5"). Interestingly, ER-phagy adaptor proteins RTN3 and ATL3 were significantly more abundant in ATG5 KO and less abundant in VAMP7 KO secretomes (Figures 4F and 4G; Table S2, secretome: filter "DOWN V7" and "UP ATG5"; RTN3 and ATL3 are the two top proteins following this criterion). In addition, we found 483 secreted proteins classified as "extracellular vesicular exosome" (Table S2, secretome: filter "extracellular vesicular exosome" from column "GOCC name"). Of these 483 proteins, 68 are significantly "UP" or "DOWN" in VAMP7 KO and 73 in ATG5 KO, indicating effect of both KOs on the secretion of exosomal proteins. When we compared ATG5 and VAMP7 KO secretomes, RTN1, CALCOCO1, ATL1, SQSTM1/p62, MAP1LC3B/LC3b, RTN4, MAP1LC3A/LC3a, GABARAPL2, RTN3, and ATL3 appeared significantly more abundant in ATG5 KO (Figure 4H; Table S2). According to published reports, a block in macroautophagy can lead to the activation of chaperone-mediated autophagy (CMA) (Kaushik et al., 2008). We specifically searched for KFERQ-containing proteins as markers of the CMA pathway (Kirchner et al., 2019; Sahu et al., 2011), but we did not find any that would be significantly enriched in ATG5 KO and decreased in VAMP7 KO secretome (Table S2, secretome: filter "DOWN V7" and "UP ATG5" and sort KFERQ using filter in CMA column). In conclusion, we found that VAMP7 KO and ATG5 KO, which have opposite effects on neurite growth, had clear opposite effects only in the secretion of RTN3 and ATL3, which are related to ER-phagy.

VAMP7 Mediates Autophagy-Stimulated Unconventional Secretion of RTN3

Next, we confirmed our prior results by performing western blotting of the cell lysates and the secretomic fractions. WT, VAMP7 KO, and ATG5 KO PC12 cells were either differentiated using NGF or left undifferentiated; thereafter, they either remained untreated or were treated with rapamycin or bafilomycin A1. ATG5 KO cells showed a very strong p62 accumulation and a virtual absence of LC3-II (Figures 5A and 5E, left, and S5A, S5B, S5D, and S5E); thus, they were fully autophagy impaired as expected. The accumulation of p62 in ATG5 KO cells indicated that p62 degradation in autophagolysosomes, which requires ATG5 for their biogenesis (Rubinsztein et al., 2012), is the main mechanism of p62 catabolism. The level of p62 was not significantly affected by rapamycin and slightly increased by bafilomycin A1 in WT and VAMP7 KO cells (Figures 5A and 5E, left, and S5A and S5D). Rapamycin did not have a robust effect on LC3-II in both WT and VAMP7 KO cells. Only bafilomycin A1, an autophagic flux inhibitor (Mauvezin and Neufeld, 2015), significantly increased LC3-II in both genotypes, suggesting that autophagic flux was high in both (Figures 5A and 5E, left, and S5B and S5E). Furthermore, the persistence of the effect of bafilomycin A1 in VAMP7 KO cells indicated that autophagosome formation and autophagosome-lysosome fusion could still proceed in the absence of VAMP7. The main band that we could detect of RTN3 in PC12 cells had an apparent molecular weight (MW) slightly below 25 kDa (Figures 5A and 5E, left) and thus corresponds to RTN3A1, one of the short isoforms (Di Scala et al., 2005). We did not observe significant effects of the tested drugs on RTN3 expression levels in either KO cell lines (Figures 5A and 5E, left, and S5C and S5F).

For western blot analysis of the secretome, which includes both soluble secreted proteins and proteins associated with secreted EVs, we first precipitated the conditioned medium using acetone to get the total protein content, an approach similar to the secretome analysis by proteomics described above. By analyzing the acetone-precipitated secreted amount as a fraction of the total content (so-called fractional release), we confirmed the proteomic analysis carried out in NGF-treated cells and found that loss of VAMP7 decreased secretion of

Figure 5. Western Blot Analysis of VAMP7 KO and ATG5 KO PC12 Cell Lysates and Secretomes

(A–D) WT, VAMP7 KO, and ATG5 KO PC12 were differentiated with NGF for 1 week and then treated with DMSO as control, Rapa (100 nM), or bafilomycin A1 (Baf; 100 nM) overnight. (A) Left: equal amounts of cell lysate proteins were processed for SDS-PAGE/western blot analysis and loaded in a gel. Right: the corresponding secretomes were precipitated with acetone, resuspended with equal volumes of lysis buffer, and equal amounts relative to input were processed for SDS-PAGE and western blot analysis. (B–D) Fractional release (secreted fraction/cell lysate) of p62 (B), LC3-II (C), and RTN3 (D) was estimated by densitometry analysis of the corresponding bands from three independent experiments. The p values show the differences among the genotypes and drug treatments after a one-way ANOVA test.

(E–H) Undifferentiated WT, VAMP7 KO, and ATG5 KO PC12 were treated with DMSO as control, Rapa (100 nM), or Baf (100 nM) overnight. (E) Left: equal amounts of cell lysate proteins were loaded, processed for SDS-PAGE, and western blot analysis. Right: the corresponding secretomes were centrifuged at 15,000 × *g* to recover larges EVs, the pellets were resuspended with equal volumes of lysis buffer, and equal volumes relative to input were processed for SDS-PAGE and western blot analysis. (F–H) Fractional release (secreted fraction/cell lysate) of p62 (B), LC3-II (C), and RTN3 (D) was estimated by densitometry analysis. The p values show the differences among the genotypes and drug treatments after a one-way ANOVA test. In all cases, the membranes were probed to detect the indicated proteins p62, GAPDH, RTN3, LC3 (A and E) and VAMP7 (E). The position of MW markers is indicated. (A and E) Western blot representative from four independent experiments are displayed.

(I) WT PC12 were differentiated for 7 days with the conditioned medium obtained from serum-free differentiation media WT, ATG5 KO, or VAMP7 KO PC12 cells. After the treatment, cells were fixed and processed for immunocytochemistry. Neurites were visualized by tubulin staining.

(J) Boxplot showing the length of the single longest neurite in PC12 cells shown in (D) (ANOVA orthogonal contrast).

RTN3, while ATG5 KO increased it (Figures 5A, right, and 5D). The effects of VAMP7 KO and ATG5 KO on p62 secretion were not significant (Figures 5A, right, and 5B). The secreted fraction only increased proportionally to the cellular content in the case of ATG5 KO. LC3-II was barely detectable in the secretome of VAMP7 KO cells (Figure 5A, right), and we could not observe any significant difference (Figure 5C), likely because the signal was too low for proper quantification. In agreement with input levels (Figures S5B and S5E), LC3-II was virtually absent in ATG5 KO secretomes, which enables quantification of fraction release for this genotype.

In order to gain precision in the quantification of secretion of RTN3, a membrane-associated protein, we then precipitated the conditioned medium at 15,000 × *g* (15K) to recover large EVs content. We used untreated PC12 cells in order to obtain large amounts. Based on Ponceau staining, we estimated that proteins secreted in large EVs corresponded to ~15%–20% of the total secreted proteins, both in NGF-treated and untreated cells (Figure S5G). The secretion of p62 was greatly enhanced in bafilomycin-A1-treated WT but much less in VAMP7 KO cells (Figures 5E, right, and 5F), indicating that VAMP7 is required for the secretion of p62 when its degradation is impaired. Interestingly, ATG5 KO did not affect the release of p62, in agreement with the notion that ATG5 is required to capture p62 in membrane structures (Romanov et al., 2012). We were able to identify LC3-II in the 15K fraction secreted by WT cells, particularly following bafilomycin A1 treatment, and the amount was greatly decreased in the same condition in VAMP7 KO cells (Figures 5E, right, and 5G). Secreted LC3-II was impossible to detect in ATG5 KO cells, as previously mentioned (data not shown in Figure 5G). The secretion of LC3-II in the 15K fractions was strongly affected by VAMP7 KO in bafilomycin-A1-treated cells. We confirmed the presence of RTN3 in the 15K fractions and the effect of VAMP7 and ATG5 KO, which decreased and increased, respectively, the amounts of RTN3 (Figures 5E, right, and 5H). In the secretome of both WT and ATG5 KO cells, we detected the full-length VAMP7 and a 15-kDa fragment likely corresponding to the cytoplasmic domain of VAMP7 as our antibody was generated against this domain (Figures 5A and 5E, right) (Verraes et al., 2018), a domain that was shown to contain a LIR (Gu et al., 2019).

Altogether, biochemical analysis of the secretome of PC12 cells clearly indicated that VAMP7 was required for the release of RTN3, p62, and LC3-II in large EVs and that ATG5 KO released more RTN3 than WT cells.

We next characterized the subcellular localization of endogenous RTN3 using immunocytochemistry in NGF-differentiated WT, VAMP7 KO, and ATG5 KO PC12 cells. We carried out double RTN3 and CD63 staining because CD63 is a marker of secretory late endosomes (Kowal et al., 2014) previously shown to co-localize with VAMP7 in PC12 cells (Coco et al., 1999). We found a rare but still distinguishable pool of membrane structures positive for both RTN3 and CD63 in WT cells (less than 5% CD63 in RTN3, less than 2% RTN3 in CD63 staining, as estimated following 3D particle detection; Figures S6A–S6C). The occurrence of CD63 in RTN3 staining was affected both by VAMP7 and ATG5 KO (Figures S6A–S6C). We think that this is a strong indication that RTN3/CD63 co-localization depends on both degradative and secretory ER-phagy.

Next, we asked whether VAMP7- and ATG5-dependent secretomes could participate in a signaling mechanism involved in neurite growth. To answer this question, we first collected medium conditioned by NGF-treated WT, VAMP7 KO, and ATG5 KO PC12 cells. We then treated naive WT PC12 cells with these different conditioned media and measured maximal neurite length. VAMP7 KO conditioned medium showed no significant effect, whereas ATG5 KO conditioned medium had slight but significant inhibitory effect (Figures 5I and 5J). Therefore, the role of VAMP7-dependent secretion did not appear to depend on a paracrine mechanism but to be rather cell autonomous. The increased secretion of ATG-related proteins in ATG5 KO might have inhibitory effects on neurite growth in addition to the cell autonomous overgrowth observed in ATG5 KO PC12 cells.

Role of VAMP7 in Nutrient-Deprived Neurons and RTN3 Subcellular Localization

We then asked whether acute inactivation of VAMP7 in neurons could prevent the effect of autophagy modulation on axonal growth. In order to acutely inhibit VAMP7-dependent functions without altering VAMP7 expression, we generated a VHH antibody, corresponding to the variable region of a heavy chain of a camelid antibody directed against the cytoplasmic domain of VAMP7 by phage display (see STAR Methods). We characterized the clone F1.1, one of the positive clones, by yeast two-hybrid assay and immunocytochemistry, showing that this nanobody specifically bound to and co-localized with VAMP7, but not VAMP2, VAMP4, Sec22, or GFP (Figures S7A–S7G). When we expressed mCherry-F1.1 as an intrabody in 2 DIV hippocampal neurons, we found a complete inhibition of the effect of nutrient restriction in axonal length compared with neurons expressing mCherry alone (Figures 6A and 6B). In previous work, we and others showed that acute expression of the auto-inhibitory Longin domain of VAMP7 had a profound effect on axonal growth (Martinez-Arca et al., 2001) and inhibited VAMP7-dependent secretion (Gupton and Gertler, 2010). Here, we expressed RFP or RFP-Longin in 2 DIV cultured neurons either left untreated or treated with rapamycin. We found that rapamycin treatment induced large punctae of RTN3 in control RFP-expressing neurons, but not in RFP-Longin-expressing neurons. Instead, we found a reticular staining of RTN3, reminiscent of ER sheets in rapamycin-treated RFP-Longin-expressing neurons (Figure 6C). Altogether, these results suggest that axonal overgrowth induced by nutrient restriction required VAMP7 and that inhibiting VAMP7-dependent secretion impaired the subcellular localization of RTN3, further strengthening the relationship between VAMP7 and RTN3.

DISCUSSION

Here, we found that nutrient restriction and autophagy modulation impacted axonal growth via a VAMP7- and autophagy-dependent secretion of ER LIR-containing proteins Reticulons and Atlastins. By showing the role of VAMP7 in both ER-phagy and exocytosis-mediated neurite growth, we have bridged two yet unconnected cellular pathways.

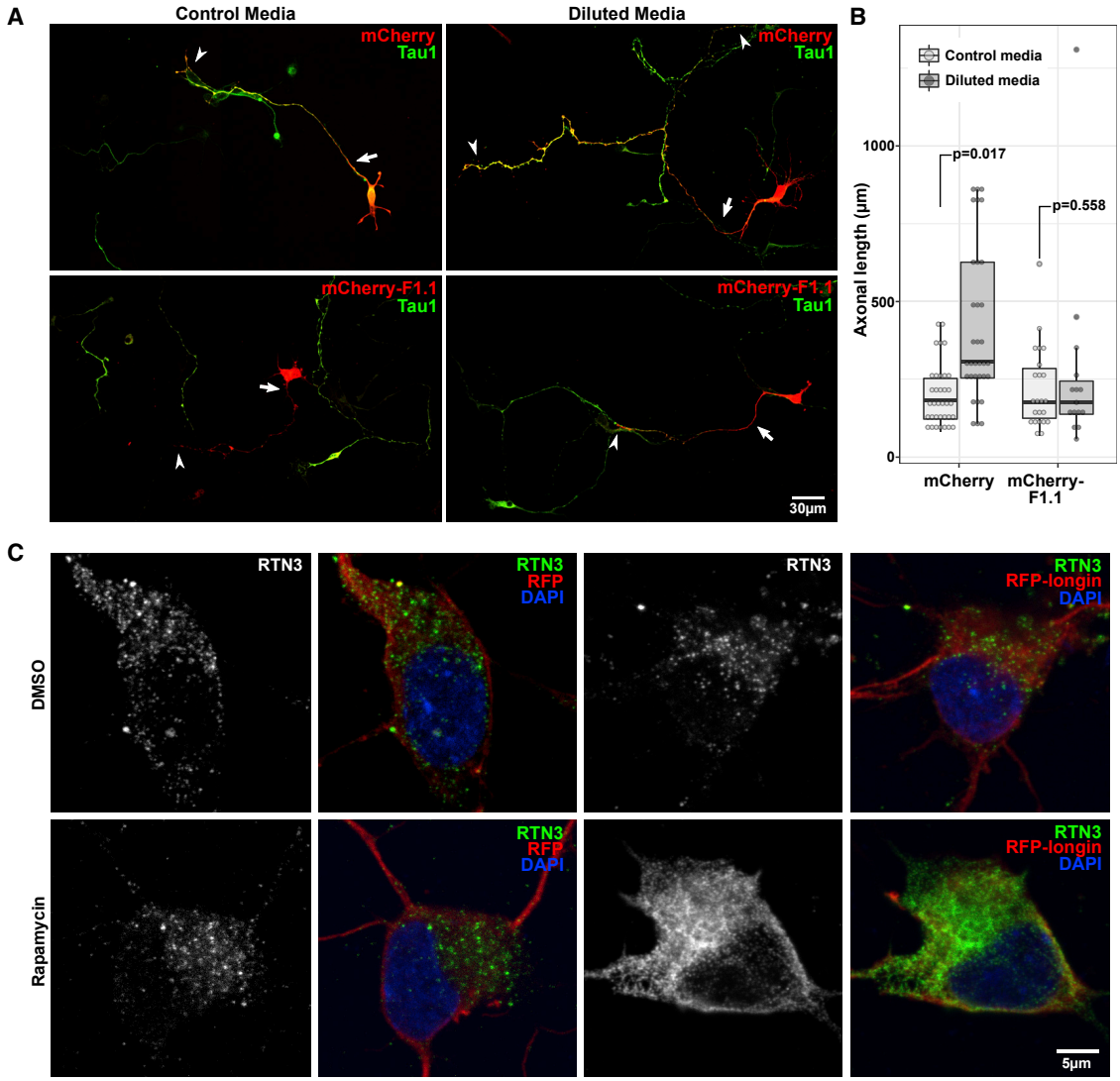

Figure 6. Role of VAMP7 in Nutrient Restriction-Induced Axonal Overgrowth and RTN3 Subcellular Localization in Hippocampal Neurons

(A) Images of hippocampal neurons transfected with a mCherry-tagged nanobody directed against VAMP7 (clone F1.1) or mCherry as a control and either left unstarved or starved for 24 h. Arrows indicate the beginning of an axon, and arrowheads point to the ends.

(B) Boxplot of the quantification of the total axonal length of transfected and starved hippocampal neurons (Student's t test).

(C) Images of hippocampal neurons transfected with RFP as a control or RFP-Longin and treated with Rapa (100 nM) or without Rapa for 4 h. Grayscale displays of RTN3 staining are shown in left panels.

Role of Autophagy in Neurite Growth

Here, we found that autophagy activation by nutrient restriction, rapamycin, Torin1, or resveratrol and autophagy inhibition by Spautin-1 or by knocking out ATG5 trigger different modalities of neurite overgrowth. The fact that nutrient restriction and several drugs that induce autophagy by direct (rapamycin, Torin1) or indirect (resveratrol) inhibition of mTOR (Zhou et al., 2010) showed similar effects on neurite growth clearly indicates that the effect was related to autophagy. The effect of nutrient restriction and autophagy induction was limited to overgrowth of the axon in neurons and the longest process in NGF-differentiated PC12 cells. The positive effect on axonal growth of nutrient restriction was not due to a change in Glc concentration as this was maintained constant and was not due to insulin limitation because we specifically tested the effect of diluting only insulin. Future studies should address the specific components of the diluted nutrients that trigger this response in neurons. Amino acids such as Leu and Arg are certainly potential candidates for their roles in autophagy (Mordier et al., 2000; Savaraj et al., 2010).

It is intriguing that both activation and inhibition of autophagy would enhance neurite growth, but what may here appear as a paradox could be explained in the context of neuronal polarity and neurite branching. Indeed, Spautin-1 induced multipolar axons, and ATG5 KO in PC12 cells led to longer, highly branched neurites. It is conceivable that the molecular mechanisms

underlying the increased axonal extension after autophagy activation and the emergence of multiple axons (or ramified processes in PC12) after autophagy inhibition partially overlap. Both modalities of neurite growth could be due to VAMP7-dependent secretion because the overgrowth effect of rapamycin and neurite ramification were both abolished in VAMP7 KO cells. Autophagy activation increases axonal length, but it does not produce supernumerary axons, suggesting that this mechanism is at least partially independent of axonal specification. Accordingly, we found that LC3 polarized into the axon and that rapamycin enhanced the motility of LC3/VAMP7 vesicles, suggesting that autophagy might participate to axonal extension by regulating the transport of endosomes in axons versus secondary neurites. These observations might suggest that autophagy may prevent axonal overgrowth, regulate ramification, and participate to axon specification during neuronal development, in line with the notion that the molecular regulation of axonal growth and axonal specification are inter-connected (Cáceres et al., 2012). We have observed that nutrient restriction activates autophagy downstream of mTOR, which has already been associated with the regulation of cell growth, particularly in dividing cells (Jewell and Guan, 2013). Our results are in good agreement with the notion that both reduced mTOR signaling and excess activation of mTOR signaling cause abnormal development of neurons (Takei and Nawa, 2014).

Role of VAMP7-Dependent Secretory ER-Phagy in Neurite Growth

Our previous work and that of others suggested an important role of VAMP7-dependent secretion in neuronal development (Alberts et al., 2003; Burgo et al., 2012, 2013; Colombo et al., 2014; Fuschini et al., 2018; Gupton and Gertler, 2010; Jausoro and Marzolo, 2021; Martinez-Arca et al., 2000, 2001). These results were based on mRNA silencing approaches and expression of the auto-inhibitory Longin domain in cultured neurons and NGF-treated PC12 cells. The VAMP7 KO mouse had a smaller brain, similar to several autophagy-deficient mouse models (Takei and Nawa, 2014), but VAMP7$^{-/-}$ neurons were still able to develop *in vitro* (Danglot et al., 2012). It is possible that other secretory pathways, particularly those involving VAMP4 or Sec22b (Colombo et al., 2014; Grassi et al., 2015; Petkovic et al., 2014), could compensate for the lack of VAMP7 in −/− neurons in culture. VAMP7 was already associated to secretory late endosomes and lysosomes in PC12 cells (Coco et al., 1999) and sensory neurons in which it is involved in the transport of the cold-sensing receptor TRPM8 (Ghosh et al., 2016). Here, using intrabody transfection, we were able to circumvent the potential functional compensation that might occur in the mouse KO neurons. Using this approach, we found an important role of VAMP7 in axonal growth when nutrient restriction conditions were applied shortly after transfection of an intrabody targeted against VAMP7. These data are in good agreement with the decreased neurite growth observed in NGF-treated VAMP7 KO PC12 cells, the lack of effect of rapamycin on neurite growth, and the rescue effect on neurite extension by re-expressing VAMP7 in VAMP7 KO PC12 cells. Part of the role of VAMP7 in neurite growth is certainly related to its involvement in the cell surface transport of L1-CAM (Alberts et al., 2003) and the Glc transporter Glut1 (Hesketh et al., 2014). Surface expression of Glut1 was shown to be stimulated by autophagy (Roy et al., 2017). Furthermore, VAMP7 exocytosis is regulated by Netrin-1 (Winkle et al., 2014) and its receptor *DCC* (Cotrufo et al., 2011). Netrin-1 activates mTOR (Bai et al., 2017) and UNC-5, the netrin receptor in the nematode, is related to UNC-51, a Ser/Thr kinase homologous to yeast Atg1, which is required for autophagy (Ogura and Goshima, 2006). Altogether, data herein and in previous publications suggest that VAMP7-mediated secretion could be strongly dependent on the metabolic state of the cell.

Here, we found that VAMP7 KO cells were defective in the secretion of p62, LC3-II, and RTN3 in large EVs. In addition, expressing the Longin domain, which was previously found to inhibit axonal growth and VAMP7-dependent exocytosis (Gupton and Gertler, 2010; Martinez-Arca et al., 2001), affected the subcellular localization of RTN3, further strengthening the relationship between VAMP7 and RTN3. The abnormal subcellular localization of RTN3 in neurons expressing RFP-Longin and treated with rapamycin likely reflects a dysfunctional ER (Sharoar et al., 2016). RTN3 is particularly interesting in relation with neurite growth because its overexpression was associated with dystrophic neurites (Hu et al., 2007). The main form of RTN3 that we recovered in the secretome corresponds to RTN3A1, a short form that has not been associated to degradative ER-phagy in contrast to the long form (Grumati et al., 2017), suggesting that degradative and non-degradative autophagy-related processes may participate in different aspects of neuronal development. It is tempting to further speculate that long forms of RTN3 could be associated with degradative ER-phagy as previously shown (Grumati et al., 2017) and short forms with secretory ER-phagy (this study), providing an interesting control checkpoint between different autophagy-related processes. When degradation in autolysomes is inhibited by loss of ATG5 or bafilomycin A1 treatment, neuronal cells would ramp up a VAMP7-dependent secretory mechanism to eliminate Reticulons and Atlastins (Figure 7).

Reticulons form tubular ER membrane structures (Voeltz et al., 2006) and ER tubules, which are relatively poor in ribosomes (Shibata et al., 2006). These might also accumulate integral membrane proteins and be connected to lipid synthesis (West et al., 2011). In addition, RTN3 regulates ER-to-Golgi transport (Wakana et al., 2005), and overexpression of RTN4 was found to enhance the secretory pathway, most likely of integrins (Mukherjee and Levy, 2019). Regulating supply from the ER to the Golgi is important for neurite outgrowth (Ruhl et al., 2019). Our data suggest that VAMP7-dependent secretion of LIR-containing Reticulons and Atlastins may contribute to neurite growth in part by regulating the early secretory pathway. It is tempting to speculate that neurite growth induces a strong upregulation of the ER to sustain the increased anabolism of proteins and lipids. Eliminating some ER surplus by both VAMP7-dependent secretory and ATG5-dependent degradative ER-phagy (Figure 7) would thus appear as a fitness mechanism. Both pathways might be involved in eliminating aggregates of secretory proteins as shown in the case of misfolded proinsulin and collagen aggregates (Cunningham et al., 2019; Omari et al., 2018) or preventing the occurrence of RTN3-mediated dystrophic neurites (Hu et al., 2007).

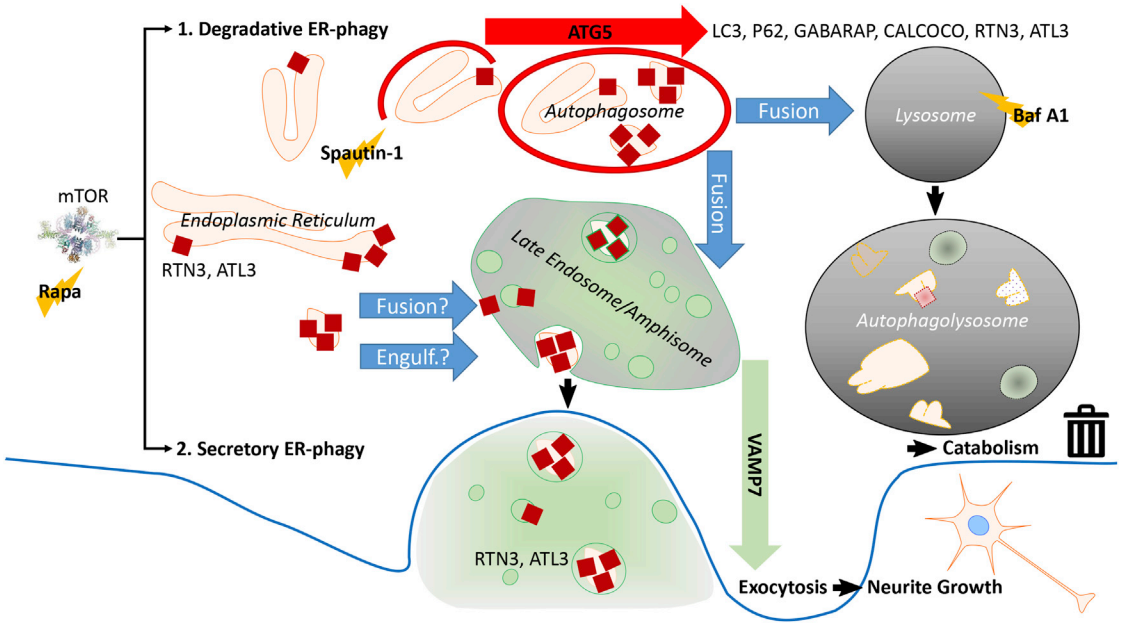

Figure 7. Working Model of ATG5- and VAMP7-Dependent ER-Phagy Pathways

Fragments of the ER may be degraded by an ATG5-dependent autophagy mechanism (1. Degradative ER-phagy—top part of the model, red arrow), allowing for the catabolism of LC3, p62, GABARAP, CALCOCO, RTN3, and ATL3. Alternatively, ER fragments and associated proteins Reticulons and Atlastins (RTN3 and ATL3, red box) may be incorporated into secretory structures such as late endosomes/amphisomes (2. Secretory ER-phagy—bottom part of the model, green arrow). ER fragments could become associated with late endosomes/amphisomes via the fusion of ER-derived vesicle or engulfment (engulf.) in nascent intraluminal vesicles of late endosomes/amphisomes. Late endosome/amphisome fuse with the plasma membrane in a VAMP7-dependent manner releasing Reticulons in membranous structures as we have shown in Figure 5. If the degradative route is inhibited by Spautin-1 or in ATG5 KO, catabolism is impaired, secretory ER-phagy (pathway 2) would still be active and generate longer and more ramified neurites as shown here. If secretory ER-phagy is impaired by VAMP7 KO, the degradative route would still be active at the same time as neurite growth is impaired. Inhibition of mTOR by Rapa would activate both 1. Degradative ER-phagy and 2. VAMP7-dependent secretory ER-phagy. Degradative ER-phagy would be involved in preventing overgrowth and controlling branching, while secretory ER-phagy would be positively involved in growth.

Both VAMP7 KO and ATG5 KO showed lipidome defects. ATG5 KO cells showed increased GluCers and increased neurite length in agreement with a previous report on the inhibitory effects of GluCer synthase inhibitor on neurite outgrowth in PC12 cells (Mutoh et al., 1998). VAMP7 KO cells exhibited reduced levels of PE. Both ceramides (Jiang and Ogretmen, 2014) and PE (Rockenfeller et al., 2015) participate in autophagy and in ER-phagy related to ER stress (Ellert-Miklaszewska et al., 2020; Viswanath et al., 2018). ATG8 proteins such as LC3 are recruited and conjugated to PE on the autophagic membrane (Thukral et al., 2015). Therefore, VAMP7's function in autophagy-dependent neurite growth could be related to transport of lipids and the recruitment of ATG8 molecules to secretory late endosomes and to the growing neurite.

We recovered large amounts of RTN3 in EVs and found the occurrence of a small subset of co-localized RTN3 and CD63 in WT cells. To be released in EVs, RTN3 would need to enter luminal vesicles of $CD63^+$ late endosomes after the fusion of ER-derived vesicles with the limiting membrane of late endosomes or via the engulfment of ER-vesicles inside the late endosomes (Figure 7). VAMP7 interacts with the ER-SNAREs SNAP47 and Syntaxin5 (Kuster et al., 2015; Siddiqi et al., 2006); thus, ER-late endosome fusion is certainly a viable hypothesis that will require further investigation. We found high amounts of LC3-II, RTN3, and VAMP7 cytosolic domain in secreted membranes pelleting at 15K, particularly following bafilomycin A1 treatment. This suggests that these membranes have a buoyancy much larger than typical exosomes that are recovered at 100,000 × *g* (Bobrie et al., 2012) and that these EVs contain cytosolic proteins (i.e., the cytoplasmic domain of VAMP7). Thus, engulfment of RTN3-containing ER-derived membranes in late endosomes as it was observed in the case of $Sec62^+$ membranes (Loi et al., 2019) appears as a likely mechanism of recruitment of RTN3 into EVs. Regardless, we exclude the possibility that released RTN3 would originate from plasma membrane shedding because we found no evidence of VAMP7-dependent release of abundant plasma membrane proteins in the extracellular medium (Table S2). Our evidence of VAMP7-dependent secretion of LC3-II further suggests that VAMP7 mediates the secretory mechanism recently revealed in non-neuronal cells (Leidal et al., 2020). The fact that bafilomycin A1 increased the release of p62, LC3-II, and RTN3 in a VAMP7-dependent manner further suggests that VAMP7 might mediate the release of amphisomes, which results from autophagosome-late endosome fusion (Figure 7).

We did not find any significant effect of culture medium conditioned by VAMP7 KO compared with WT cells on neurite growth of naive cells. This suggests that the mechanisms

unraveled here are primarily cell autonomous, but it still does not exclude the possibility of autocrine effects or paracrine effects at short distances, particularly in the context of the presence of RNA-binding proteins in LC3-II-positive EVs (Leidal et al., 2020). In fact, the inhibitory effect of the ATG5 KO secretome on neurite growth may suggest that the lack of degradative autophagy profoundly deregulates neurite growth with both cell-autonomous neurite overgrowth and non-cell-autonomous inhibition of growth. Our results are in good agreement with the recent finding that a proteolytic C-terminal fragment of Reticulon 4A is released in exosomes and inhibits axon regeneration (Sekine et al., 2020). Further characterization of the biochemical content of these secreted membranes may reveal their autocrine or paracrine effects on specific cellular functions.

In conclusion, our findings suggest that endosomes can mediate the release of ER-phagy elements such as Reticulons and Atlastins in a VAMP7-dependent manner during neurite growth and neuronal polarization. Further studies will be important not only in the context of brain development but also for brain function after development, particularly because Reticulons and Atlastins have largely been associated with neurodegenerative diseases (Yamanaka and Nukina, 2018) and VAMP7 with sex-related disease in humans (Chávez-López et al., 2020; Tannour-Louet et al., 2014). Our findings further add secretory ER-phagy as a route of unconventional secretion.

STAR★METHODS

Detailed methods are provided in the online version of this paper and include the following:

- KEY RESOURCES TABLE
- RESOURCE AVAILABILITY
  - Lead Contact
  - Materials Availability
  - Data and Code Availability
- EXPERIMENTAL MODEL AND SUBJECT DETAILS
  - Cell lines
  - Primary cultures
- METHOD DETAILS
  - Cell treatments with chemicals
  - Protein electrophoresis and western blot
  - Secretome fractionation
  - Lipidomic analysis
  - Proteomic analysis
  - Immunofluorescence and microscopic imaging
  - CRISPR/Cas9 genetic engineering
  - Selection of the VHHs against VAMP7
- QUANTIFICATION AND STATISTICAL ANALYSIS
  - Image analysis
  - Statistical analysis

SUPPLEMENTAL INFORMATION

Supplemental Information can be found online at https://doi.org/10.1016/j.celrep.2020.108536.

ACKNOWLEDGMENTS

We thank Eric Chevet, Somya Vats, Sharon Tooze, and Guillaume van Niel for critical reading of the manuscript and helpful discussion and Somya Vats for final editing. We thank all members of the laboratory for their assistance and discussions. Work in our group was funded by grants from Association Française contre les Myopathies (16612), the French National Research Agency (*NeuroImmunoSynapse* ANR-13-BSV2-0018-02; *MetDePaDi* ANR-16-CE16-0012), the Institut National Du Cancer (PLBIO 2018-149), the Fondation pour la Recherche Médicale (FRM, Labélisation T Galli), Who am I? Labex (Idex ANR-11-IDEX-0005-01), and awards of the Association Robert Debré pour la Recherche Médicale and Fondation Bettencourt-Schueller to T.G. Collaborative grants associating T.G. and M.I.C. were from ECOS-Sud-Collaborative Project (A13S02 MINCyT-ECOS) and Idex USPC (ANR-11-IDEX-0005, "Conventional and Unconventional Secretion in Neurite Growth"). Imaging was carried out at NeurImag Imaging core facility, part of the IPNP, INSERM U1266, Université de Paris. We thank Leducq Foundation (LEDUCQ RE-TP_2016_U894_GALLI_TANTER) for funding the Leica SP8 Confocal/STED 3DX system. We acknowledge B&B technological core facility of IPNP for technical support and the ImagoSeine core facility of the Institut Jacques Monod, member of the France BioImaging (ANR-10-INBS-04), for their services.

AUTHOR CONTRIBUTIONS

Conceptualization, J.W., S.N., and T.G.; Methodology, J.W., S.N., B.C., I.C.G., and G.S.; Investigation, J.W. S.N., B.C., P.B., F.F., J.L., S.M.L., J.N., A.S., A.O., C.M.F., and T.G.; Data Analysis, J.W., S.N., M.T.P., S.M.L., G.S., I.C.G., and T.G.; Writing – Original Draft, J.W., S.N., and T.G.; Funding Acquisition, T.G.; Supervision, C.M.F., M.I.C., I.C.G., and T.G.

DECLARATION OF INTERESTS

The authors declare no competing interests.

Received: August 24, 2019
Revised: October 28, 2020
Accepted: November 25, 2020
Published: December 22, 2020

REFERENCES

Alberts, P., Rudge, R., Hinners, I., Muzerelle, A., Martinez-Arca, S., Irinopoulou, T., Marthiens, V., Tooze, S., Rathjen, F., Gaspar, P., and Galli, T. (2003). Cross talk between tetanus neurotoxin-insensitive vesicle-associated membrane protein-mediated transport and L1-mediated adhesion. Mol. Biol. Cell *14*, 4207–4220.

Aoyagi, K., Itakura, M., Fukutomi, T., Nishiwaki, C., Nakamichi, Y., Torii, S., Makiyama, T., Harada, A., and Ohara-Imaizumi, M. (2018). VAMP7 Regulates Autophagosome Formation by Supporting Atg9a Functions in Pancreatic β-Cells From Male Mice. Endocrinology *159*, 3674–3688.

Bai, L., Mei, X., Shen, Z., Bi, Y., Yuan, Y., Guo, Z., Wang, H., Zhao, H., Zhou, Z., Wang, C., et al. (2017). Netrin-1 Improves Functional Recovery through Autophagy Regulation by Activating the AMPK/mTOR Signaling Pathway in Rats with Spinal Cord Injury. Sci. Rep. *7*, 42288.

Birgisdottir, Å.B., Lamark, T., and Johansen, T. (2013). The LIR motif - crucial for selective autophagy. J. Cell Sci. *126*, 3237–3247.

Bobrie, A., Colombo, M., Krumeich, S., Raposo, G., and Théry, C. (2012). Diverse subpopulations of vesicles secreted by different intracellular mechanisms are present in exosome preparations obtained by differential ultracentrifugation. J. Extracell. Vesicles *1*, 10.3402/jev.v1i0.18397.

Boya, P., Reggiori, F., and Codogno, P. (2013). Emerging regulation and functions of autophagy. Nat. Cell Biol. *15*, 713–720.

Bradke, F., and Dotti, C.G. (2000). Differentiated neurons retain the capacity to generate axons from dendrites. Curr. Biol. *10*, 1467–1470.

Burgo, A., Proux-Gillardeaux, V., Sotirakis, E., Bun, P., Casano, A., Verraes, A., Liem, R.K.H., Formstecher, E., Coppey-Moisan, M., and Galli, T. (2012). A molecular network for the transport of the TI-VAMP/VAMP7 vesicles from cell center to periphery. Dev. Cell *23*, 166–180.

Burgo, A., Casano, A.M., Kuster, A., Arold, S.T., Wang, G., Nola, S., Verraes, A., Dingli, F., Loew, D., and Galli, T. (2013). Increased activity of the vesicular soluble N-ethylmaleimide-sensitive factor attachment protein receptor TI-VAMP/VAMP7 by tyrosine phosphorylation in the Longin domain. J. Biol. Chem. *288*, 11960–11972.

Cáceres, A., Ye, B., and Dotti, C.G. (2012). Neuronal polarity: demarcation, growth and commitment. Curr. Opin. Cell Biol. *24*, 547–553.

Chari, R., Yeo, N.C., Chavez, A., and Church, G.M. (2017). sgRNA Scorer 2.0: A Species-Independent Model To Predict CRISPR/Cas9 Activity. ACS Synth. Biol. *6*, 902–904.

Chávez-López, S., de Jesús Lugo-Trampe, J., Ibarra-Ramírez, M., Calvo-Anguiano, G., Martínez-de-Villarreal, L.E., and Campos-Acevedo, L.D. (2020). A case series of infants with increased vamp7 gene dosage at birth and virilization defects. J. Pediatr. Urol. *16*, 423.e1–423.e6.

Chenouard, N., Bloch, I., and Olivo-Marin, J.-C. (2013). Multiple hypothesis tracking for cluttered biological image sequences. IEEE Trans. Pattern Anal. Mach. Intell. *35*, 2736–3750.

Coco, S., Raposo, G., Martinez, S., Fontaine, J.J., Takamori, S., Zahraoui, A., Jahn, R., Matteoli, M., Louvard, D., and Galli, T. (1999). Subcellular localization of tetanus neurotoxin-insensitive vesicle-associated membrane protein (VAMP)/VAMP7 in neuronal cells: evidence for a novel membrane compartment. J. Neurosci. *19*, 9803–9812.

Colombo, F., Racchetti, G., and Meldolesi, J. (2014). Neurite outgrowth induced by NGF or L1CAM via activation of the TrkA receptor is sustained also by the exocytosis of enlargeosomes. Proc. Natl. Acad. Sci. USA *111*, 16943–16948.

Cotrufo, T., Pérez-Brangulí, F., Muhaisen, A., Ros, O., Andrés, R., Baeriswyl, T., Fuschini, G., Tarrago, T., Pascual, M., Ureña, J., et al. (2011). A signaling mechanism coupling netrin-1/deleted in colorectal cancer chemoattraction to SNARE-mediated exocytosis in axonal growth cones. J. Neurosci. *31*, 14463–14480.

Cox, J., and Mann, M. (2008). MaxQuant enables high peptide identification rates, individualized p.p.b.-range mass accuracies and proteome-wide protein quantification. Nat. Biotechnol. *26*, 1367–1372.

Cunningham, C.N., Williams, J.M., Knupp, J., Arunagiri, A., Arvan, P., and Tsai, B. (2019). Cells Deploy a Two-Pronged Strategy to Rectify Misfolded Proinsulin Aggregates. Mol. Cell *75*, 442–456.e4.

Danglot, L., Zylbersztejn, K., Petkovic, M., Gauberti, M., Meziane, H., Combe, R., Champy, M.-F., Birling, M.-C., Pavlovic, G., Bizot, J.-C., et al. (2012). Absence of TI-VAMP/Vamp7 leads to increased anxiety in mice. J. Neurosci. *32*, 1962–1968.

de Chaumont, F., Dallongeville, S., Chenouard, N., Hervé, N., Pop, S., Provoost, T., Meas-Yedid, V., Pankajakshan, P., Lecomte, T., Le Montagner, Y., et al. (2012). Icy: an open bioimage informatics platform for extended reproducible research. Nat. Methods *9*, 690–696.

Di Scala, F., Dupuis, L., Gaiddon, C., De Tapia, M., Jokic, N., Gonzalez de Aguilar, J.-L., Raul, J.-S., Ludes, B., and Loeffler, J.-P. (2005). Tissue specificity and regulation of the N-terminal diversity of reticulon 3. Biochem. J. *385*, 125–134.

Dotti, C.G., Sullivan, C.A., and Banker, G.A. (1988). The establishment of polarity by hippocampal neurons in culture. J. Neurosci. *8*, 1454–1468.

EauClaire, S., and Guo, W. (2003). Conservation and specialization. The role of the exocyst in neuronal exocytosis. Neuron *37*, 369–370.

Ellert-Miklaszewska, A., Ciechomska, I.A., and Kaminska, B. (2020). Cannabinoid signaling in glioma cells. Adv. Exp. Med. Biol. *1202*, 223–241.

Fader, C.M., Aguilera, M.O., and Colombo, M.I. (2012). ATP is released from autophagic vesicles to the extracellular space in a VAMP7-dependent manner. Autophagy *8*, 1741–1756.

Fuschini, G., Cotrufo, T., Ros, O., Muhaisen, A., Andrés, R., Comella, J.X., and Soriano, E. (2018). Syntaxin-1/TI-VAMP SNAREs interact with Trk receptors and are required for neurotrophin-dependent outgrowth. Oncotarget *9*, 35922–35940.

Ghosh, D., Pinto, S., Danglot, L., Vandewauw, I., Segal, A., Van Ranst, N., Benoit, M., Janssens, A., Vennekens, R., Vanden Berghe, P., et al. (2016). VAMP7 regulates constitutive membrane incorporation of the cold-activated channel TRPM8. Nat. Commun. *7*, 10489.

Grassi, D., Plonka, F.B., Oksdath, M., Guil, A.N., Sosa, L.J., and Quiroga, S. (2015). Selected SNARE proteins are essential for the polarized membrane insertion of igf-1 receptor and the regulation of initial axonal outgrowth in neurons. Cell Discov. *1*, 15023.

Greene, L.A., and Tischler, A.S. (1976). Establishment of a noradrenergic clonal line of rat adrenal pheochromocytoma cells which respond to nerve growth factor. Proc. Natl. Acad. Sci. USA *73*, 2424–2428.

Grumati, P., Morozzi, G., Hölper, S., Mari, M., Harwardt, M.I., Yan, R., Müller, S., Reggiori, F., Heilemann, M., and Dikic, I. (2017). Full length RTN3 regulates turnover of tubular endoplasmic reticulum via selective autophagy. eLife *6*, e25555.

Gu, Y., Princely Abudu, Y., Kumar, S., Bissa, B., Choi, S.W., Jia, J., Lazarou, M., Eskelinen, E.-L., Johansen, T., and Deretic, V. (2019). Mammalian Atg8 proteins regulate lysosome and autolysosome biogenesis through SNAREs. EMBO J. *38*, e101994.

Guo, B., Liang, Q., Li, L., Hu, Z., Wu, F., Zhang, P., Ma, Y., Zhao, B., Kovács, A.L., Zhang, Z., et al. (2014). O-GlcNAc-modification of SNAP-29 regulates autophagosome maturation. Nat. Cell Biol. *16*, 1215–1226.

Gupton, S.L., and Gertler, F.B. (2010). Integrin signaling switches the cytoskeletal and exocytic machinery that drives neuritogenesis. Dev. Cell *18*, 725–736.

Havé, M., Luo, J., Tellier, F., Balliau, T., Cueff, G., Chardon, F., Zivy, M., Rajjou, L., Cacas, J.-L., and Masclaux-Daubresse, C. (2019). Proteomic and lipidomic analyses of the Arabidopsis atg5 autophagy mutant reveal major changes in endoplasmic reticulum and peroxisome metabolisms and in lipid composition. New Phytol. *223*, 1461–1477.

Hesketh, G.G., Pérez-Dorado, I., Jackson, L.P., Wartosch, L., Schäfer, I.B., Gray, S.R., McCoy, A.J., Zeldin, O.B., Garman, E.F., Harbour, M.E., et al. (2014). VARP is recruited on to endosomes by direct interaction with retromer, where together they function in export to the cell surface. Dev. Cell *29*, 591–606.

Hu, X., Shi, Q., Zhou, X., He, W., Yi, H., Yin, X., Gearing, M., Levey, A., and Yan, R. (2007). Transgenic mice overexpressing reticulon 3 develop neuritic abnormalities. EMBO J. *26*, 2755–2767.

Ikemoto, A., and Okuyama, H. (2000). Differential utilization of the ethanolamine moiety of phosphatidylethanolamine derived from serine and ethanolamine during NGF-induced neuritogenesis of PC12 cells. Neurochem. Res. *25*, 293–301.

Itakura, E., Kishi-Itakura, C., and Mizushima, N. (2012). The hairpin-type tail-anchored SNARE syntaxin 17 targets to autophagosomes for fusion with endosomes/lysosomes. Cell *151*, 1256–1269.

Jausoro, I., and Marzolo, M.-P. (2021). Reelin activates the small GTPase TC10 and VAMP7 to promote neurite outgrowth and regeneration of dorsal root ganglia (DRG) neurons. J. Neurosci. Res. *99*, 392–406.

Jewell, J.L., and Guan, K.-L. (2013). Nutrient signaling to mTOR and cell growth. Trends Biochem. Sci. *38*, 233–242.

Jiang, W., and Ogretmen, B. (2014). Autophagy paradox and ceramide. Biochim. Biophys. Acta *1841*, 783–792.

Kabeya, Y., Mizushima, N., Yamamoto, A., Oshitani-Okamoto, S., Ohsumi, Y., and Yoshimori, T. (2004). LC3, GABARAP and GATE16 localize to autophagosomal membrane depending on form-II formation. J. Cell Sci. *117*, 2805–2812.

Kaech, S., and Banker, G. (2006). Culturing hippocampal neurons. Nat. Protoc. *1*, 2406–2415.

Kaushik, S., Massey, A.C., Mizushima, N., and Cuervo, A.M. (2008). Constitutive activation of chaperone-mediated autophagy in cells with impaired macroautophagy. Mol. Biol. Cell *19*, 2179–2192.

Kim, J., Kundu, M., Viollet, B., and Guan, K.-L. (2011). AMPK and mTOR regulate autophagy through direct phosphorylation of Ulk1. Nat. Cell Biol. *13*, 132–141.

Kirchner, P., Bourdenx, M., Madrigal-Matute, J., Tiano, S., Diaz, A., Bartholdy, B.A., Will, B., and Cuervo, A.M. (2019). Proteome-wide analysis of chaperone-mediated autophagy targeting motifs. PLoS Biol. *17*, e3000301.

Klionsky, D.J., Eskelinen, E.-L., and Deretic, V. (2014). Autophagosomes, phagosomes, autolysosomes, phagolysosomes, autophagolysosomes... wait, I'm confused. Autophagy *10*, 549–551.

Kowal, J., Tkach, M., and Théry, C. (2014). Biogenesis and secretion of exosomes. Curr. Opin. Cell Biol. *29*, 116–125.

Kuster, A., Nola, S., Dingli, F., Vacca, B., Gauchy, C., Beaujouan, J.-C., Nunez, M., Moncion, T., Loew, D., Formstecher, E., et al. (2015). The Q-soluble N-Ethylmaleimide-sensitive Factor Attachment Protein Receptor (Q-SNARE) SNAP-47 Regulates Trafficking of Selected Vesicle-associated Membrane Proteins (VAMPs). J. Biol. Chem. *290*, 28056–28069.

Lagache, T., Sauvonnet, N., Danglot, L., and Olivo-Marin, J.-C. (2015). Statistical analysis of molecule colocalization in bioimaging. Cytometry A *87*, 568–579.

Leidal, A.M., Huang, H.H., Marsh, T., Solvik, T., Zhang, D., Ye, J., Kai, F., Goldsmith, J., Liu, J.Y., Huang, Y.-H., et al. (2020). The LC3-conjugation machinery specifies the loading of RNA-binding proteins into extracellular vesicles. Nat. Cell Biol. *22*, 187–199.

Liu, J., Xia, H., Kim, M., Xu, L., Li, Y., Zhang, L., Cai, Y., Norberg, H.V., Zhang, T., Furuya, T., et al. (2011). Beclin1 controls the levels of p53 by regulating the deubiquitination activity of USP10 and USP13. Cell *147*, 223–234.

Loi, M., Raimondi, A., Morone, D., and Molinari, M. (2019). ESCRT-III-driven piecemeal micro-ER-phagy remodels the ER during recovery from ER stress. Nat. Commun. *10*, 5058.

Longair, M.H., Baker, D.A., and Armstrong, J.D. (2011). Simple Neurite Tracer: open source software for reconstruction, visualization and analysis of neuronal processes. Bioinformatics *27*, 2453–2454.

Martinez-Arca, S., Alberts, P., Zahraoui, A., Louvard, D., and Galli, T. (2000). Role of tetanus neurotoxin insensitive vesicle-associated membrane protein (TI-VAMP) in vesicular transport mediating neurite outgrowth. J. Cell Biol. *149*, 889–900.

Martinez-Arca, S., Coco, S., Mainguy, G., Schenk, U., Alberts, P., Bouillé, P., Mezzina, M., Prochiantz, A., Matteoli, M., Louvard, D., and Galli, T. (2001). A common exocytotic mechanism mediates axonal and dendritic outgrowth. J. Neurosci. *21*, 3830–3838.

Matsushita, M., Suzuki, N.N., Obara, K., Fujioka, Y., Ohsumi, Y., and Inagaki, F. (2007). Structure of Atg5.Atg16, a complex essential for autophagy. J. Biol. Chem. *282*, 6763–6772.

Matz, J., and Chames, P. (2012). Phage display and selections on purified antigens. Methods Mol. Biol. *907*, 213–224.

Mauvezin, C., and Neufeld, T.P. (2015). Bafilomycin A1 disrupts autophagic flux by inhibiting both V-ATPase-dependent acidification and Ca-P60A/SERCA-dependent autophagosome-lysosome fusion. Autophagy *11*, 1437–1438.

McLelland, G.-L., Lee, S.A., McBride, H.M., and Fon, E.A. (2016). Syntaxin-17 delivers PINK1/parkin-dependent mitochondrial vesicles to the endolysosomal system. J. Cell Biol. *214*, 275–291.

Mizushima, N., Yoshimori, T., and Ohsumi, Y. (2011). The role of Atg proteins in autophagosome formation. Annu. Rev. Cell Dev. Biol. *27*, 107–132.

Mordier, S., Deval, C., Béchet, D., Tassa, A., and Ferrara, M. (2000). Leucine limitation induces autophagy and activation of lysosome-dependent proteolysis in C2C12 myotubes through a mammalian target of rapamycin-independent signaling pathway. J. Biol. Chem. *275*, 29900–29906.

Moreau, K., Ravikumar, B., Renna, M., Puri, C., and Rubinsztein, D.C. (2011). Autophagosome precursor maturation requires homotypic fusion. Cell *146*, 303–317.

Moutel, S., Bery, N., Bernard, V., Keller, L., Lemesre, E., de Marco, A., Ligat, L., Rain, J.-C., Favre, G., Olichon, A., et al. (2016). NaLi-H1: A universal synthetic library of humanized nanobodies providing highly functional antibodies and intrabodies. Elife *5*.

Mukherjee, R.N., and Levy, D.L. (2019). Reticulon 4a promotes exocytosis in mammalian cells. Mol. Biol. Cell *30*, 2349–2357.

Mutoh, T., Tokuda, A., Inokuchi, J., and Kuriyama, M. (1998). Glucosylceramide synthase inhibitor inhibits the action of nerve growth factor in PC12 cells. J. Biol. Chem. *273*, 26001–26007.

Ogura, K., and Goshima, Y. (2006). The autophagy-related kinase UNC-51 and its binding partner UNC-14 regulate the subcellular localization of the Netrin receptor UNC-5 in Caenorhabditis elegans. Development *133*, 3441–3450.

Olivo-Marin, J.-C. (2002). Extraction of spots in biological images using multiscale products. Pattern Recognit *35*, 1989–1996.

Ollion, J., Cochennec, J., Loll, F., Escudé, C., and Boudier, T. (2013). TANGO: a generic tool for high-throughput 3D image analysis for studying nuclear organization. Bioinformatics *29*, 1840–1841.

Omari, S., Makareeva, E., Roberts-Pilgrim, A., Mirigian, L., Jarnik, M., Ott, C., Lippincott-Schwartz, J., and Leikin, S. (2018). Noncanonical autophagy at ER exit sites regulates procollagen turnover. Proc. Natl. Acad. Sci. USA *115*, E10099–E10108.

Petkovic, M., Jemaiel, A., Daste, F., Specht, C.G., Izeddin, I., Vorkel, D., Verbavatz, J.-M., Darzacq, X., Triller, A., Pfenninger, K.H., et al. (2014). The SNARE Sec22b has a non-fusogenic function in plasma membrane expansion. Nat. Cell Biol. *16*, 434–444.

Ponpuak, M., Mandell, M.A., Kimura, T., Chauhan, S., Cleyrat, C., and Deretic, V. (2015). Secretory autophagy. Curr. Opin. Cell Biol. *35*, 106–116.

Proux-Gillardeaux, V., Raposo, G., Irinopoulou, T., and Galli, T. (2007). Expression of the Longin domain of TI-VAMP impairs lysosomal secretion and epithelial cell migration. Biol. Cell *99*, 261–271.

Racchetti, G., Lorusso, A., Schulte, C., Gavello, D., Carabelli, V., D'Alessandro, R., and Meldolesi, J. (2010). Rapid neurite outgrowth in neurosecretory cells and neurons is sustained by the exocytosis of a cytoplasmic organelle, the enlargeosome. J. Cell Sci. *123*, 165–170.

Ramírez-Peinado, S., León-Annicchiarico, C.L., Galindo-Moreno, J., Iurlaro, R., Caro-Maldonado, A., Prehn, J.H.M., Ryan, K.M., and Muñoz-Pinedo, C. (2013). Glucose-starved cells do not engage in prosurvival autophagy. J. Biol. Chem. *288*, 30387–30398.

Ran, F.A., Hsu, P.D., Wright, J., Agarwala, V., Scott, D.A., and Zhang, F. (2013). Genome engineering using the CRISPR-Cas9 system. Nat. Protoc. *8*, 2281–2308.

Rockenfeller, P., Koska, M., Pietrocola, F., Minois, N., Knittelfelder, O., Sica, V., Franz, J., Carmona-Gutierrez, D., Kroemer, G., and Madeo, F. (2015). Phosphatidylethanolamine positively regulates autophagy and longevity. Cell Death Differ. *22*, 499–508.

Romanov, J., Walczak, M., Ibiricu, I., Schüchner, S., Ogris, E., Kraft, C., and Martens, S. (2012). Mechanism and functions of membrane binding by the Atg5-Atg12/Atg16 complex during autophagosome formation. EMBO J. *31*, 4304–4317.

Roy, S., Leidal, A.M., Ye, J., Ronen, S.M., and Debnath, J. (2017). Autophagy-Dependent Shuttling of TBC1D5 Controls Plasma Membrane Translocation of GLUT1 and Glucose Uptake. Mol. Cell *67*, 84–95.e5.

Rubinsztein, D.C., Shpilka, T., and Elazar, Z. (2012). Mechanisms of autophagosome biogenesis. Curr. Biol. *22*, R29–R34.

Ruhl, D.A., Bomba-Warczak, E., Watson, E.T., Bradberry, M.M., Peterson, T.A., Basu, T., Frelka, A., Evans, C.S., Briguglio, J.S., Basta, T., et al. (2019). Synaptotagmin 17 controls neurite outgrowth and synaptic physiology via distinct cellular pathways. Nat. Commun. *10*, 3532.

Sahu, R., Kaushik, S., Clement, C.C., Cannizzo, E.S., Scharf, B., Follenzi, A., Potolicchio, I., Nieves, E., Cuervo, A.M., and Santambrogio, L. (2011). Microautophagy of cytosolic proteins by late endosomes. Dev. Cell *20*, 131–139.

Savaraj, N., You, M., Wu, C., Wangpaichitr, M., Kuo, M.T., and Feun, L.G. (2010). Arginine deprivation, autophagy, apoptosis (AAA) for the treatment of melanoma. Curr. Mol. Med. *10*, 405–412.

Schindelin, J., Arganda-Carreras, I., Frise, E., Kaynig, V., Longair, M., Pietzsch, T., Preibisch, S., Rueden, C., Saalfeld, S., Schmid, B., et al. (2012). Fiji: an open-source platform for biological-image analysis. Nat. Methods *9*, 676–682.

Schneider, C.A., Rasband, W.S., and Eliceiri, K.W. (2012). NIH Image to ImageJ: 25 years of image analysis. Nat. Methods *9*, 671–675.

Sekine, Y., Lindborg, J.A., and Strittmatter, S.M. (2020). A proteolytic C-terminal fragment of Nogo-A (reticulon-4A) is released in exosomes and potently inhibits axon regeneration. J. Biol. Chem. *295*, 2175–2183.

Sharoar, M.G., Shi, Q., Ge, Y., He, W., Hu, X., Perry, G., Zhu, X., and Yan, R. (2016). Dysfunctional tubular endoplasmic reticulum constitutes a pathological feature of Alzheimer's disease. Mol. Psychiatry *21*, 1263–1271.

Shibata, Y., Voeltz, G.K., and Rapoport, T.A. (2006). Rough sheets and smooth tubules. Cell *126*, 435–439.

Siddiqi, S.A., Siddiqi, S., Mahan, J., Peggs, K., Gorelick, F.S., and Mansbach, C.M., 2nd. (2006). The identification of a novel endoplasmic reticulum to Golgi SNARE complex used by the prechylomicron transport vesicle. J. Biol. Chem. *281*, 20974–20982.

Takáts, S., Nagy, P., Varga, Á., Pircs, K., Kárpáti, M., Varga, K., Kovács, A.L., Hegedűs, K., and Juhász, G. (2013). Autophagosomal Syntaxin17-dependent lysosomal degradation maintains neuronal function in Drosophila. J. Cell Biol. *201*, 531–539.

Song, J.-W., Lam, S.M., Fan, X., Cao, W.-J., Wang, S.-Y., Tian, H., Chua, G.H., Zhang, C., Meng, F.-P., Xu, Z., et al. (2020). Omics-Driven Systems Interrogation of Metabolic Dysregulation in COVID-19 Pathogenesis. Cell Metab *32*, 188–202.e5.

Takáts, S., Glatz, G., Szenci, G., Boda, A., Horváth, G.V., Hegedűs, K., Kovács, A.L., and Juhász, G. (2018). Non-canonical role of the SNARE protein Ykt6 in autophagosome-lysosome fusion. PLoS Genet. *14*, e1007359.

Takei, N., and Nawa, H. (2014). mTOR signaling and its roles in normal and abnormal brain development. Front. Mol. Neurosci. *7*, 28.

Tamura, H., Shibata, M., Koike, M., Sasaki, M., and Uchiyama, Y. (2010). Atg9A protein, an autophagy-related membrane protein, is localized in the neurons of mouse brains. J. Histochem. Cytochem. *58*, 443–453.

Tannour-Louet, M., Han, S., Louet, J.-F., Zhang, B., Romero, K., Addai, J., Sahin, A., Cheung, S.W., and Lamb, D.J. (2014). Increased gene copy number of VAMP7 disrupts human male urogenital development through altered estrogen action. Nat. Med. *20*, 715–724.

Thukral, L., Sengupta, D., Ramkumar, A., Murthy, D., Agrawal, N., and Gokhale, R.S. (2015). The Molecular Mechanism Underlying Recruitment and Insertion of Lipid-Anchored LC3 Protein into Membranes. Biophys. J. *109*, 2067–2078.

Vega, I.E., and Hsu, S.C. (2001). The exocyst complex associates with microtubules to mediate vesicle targeting and neurite outgrowth. J. Neurosci. *21*, 3839–3848.

Verderio, C., Cagnoli, C., Bergami, M., Francolini, M., Schenk, U., Colombo, A., Riganti, L., Frassoni, C., Zuccaro, E., Danglot, L., et al. (2012). TI-VAMP/VAMP7 is the SNARE of secretory lysosomes contributing to ATP secretion from astrocytes. Biol. Cell *104*, 213–228.

Verraes, A., Cholley, B., Galli, T., and Nola, S. (2018). Comparative study of commercially available and homemade anti-VAMP7 antibodies using CRISPR/Cas9-depleted HeLa cells and VAMP7 knockout mice. F1000Res. *7*, 1649.

Viswanath, P., Radoul, M., Izquierdo-Garcia, J.L., Ong, W.Q., Luchman, H.A., Cairncross, J.G., Huang, B., Pieper, R.O., Phillips, J.J., and Ronen, S.M. (2018). 2-Hydroxyglutarate-Mediated Autophagy of the Endoplasmic Reticulum Leads to an Unusual Downregulation of Phospholipid Biosynthesis in Mutant IDH1 Gliomas. Cancer Res. *78*, 2290–2304.

Voeltz, G.K., Prinz, W.A., Shibata, Y., Rist, J.M., and Rapoport, T.A. (2006). A class of membrane proteins shaping the tubular endoplasmic reticulum. Cell *124*, 573–586.

Wakana, Y., Koyama, S., Nakajima, K., Hatsuzawa, K., Nagahama, M., Tani, K., Hauri, H.-P., Melançon, P., and Tagaya, M. (2005). Reticulon 3 is involved in membrane trafficking between the endoplasmic reticulum and Golgi. Biochem. Biophys. Res. Commun. *334*, 1198–1205.

Wang, Y., Li, L., Hou, C., Lai, Y., Long, J., Liu, J., Zhong, Q., and Diao, J. (2016). SNARE-mediated membrane fusion in autophagy. Semin. Cell Dev. Biol. *60*, 97–104.

West, M., Zurek, N., Hoenger, A., and Voeltz, G.K. (2011). A 3D analysis of yeast ER structure reveals how ER domains are organized by membrane curvature. J. Cell Biol. *193*, 333–346.

Winkle, C.C., McClain, L.M., Valtschanoff, J.G., Park, C.S., Maglione, C., and Gupton, S.L. (2014). A novel Netrin-1-sensitive mechanism promotes local SNARE-mediated exocytosis during axon branching. J. Cell Biol. *205*, 217–232.

Witte, H., Neukirchen, D., and Bradke, F. (2008). Microtubule stabilization specifies initial neuronal polarization. J. Cell Biol. *180*, 619–632.

Wojnacki, J., and Galli, T. (2016). Membrane traffic during axon development. Dev. Neurobiol. *76*, 1185–1200.

Yamanaka, T., and Nukina, N. (2018). ER dynamics and derangement in neurological diseases. Front. Neurosci. *12*, 91.

Yoshimura, T., Kawano, Y., Arimura, N., and Kawabata, S. (2005). GSK-3beta regulates phosphorylation of CRMP-2 and neuronal polarity. Cell *120*, 137–149.

Young, J.E., Martinez, R.A., and La Spada, A.R. (2009). Nutrient deprivation induces neuronal autophagy and implicates reduced insulin signaling in neuroprotective autophagy activation. J. Biol. Chem. *284*, 2363–2373.

Zhou, H., Luo, Y., and Huang, S. (2010). Updates of mTOR inhibitors. Anticancer. Agents Med. Chem. *10*, 571–581.

STAR★METHODS

KEY RESOURCES TABLE

REAGENT or RESOURCE	SOURCE	IDENTIFIER
Antibodies		
Anti LC3B	Sigma	Cat# L7543; RRID:AB_796155
Anti GAPDH	Sigma	Cat# G9545; RRID:AB_796208
Anti ULK1	Cell Signaling Technology	Cat# 8054; RRID:AB_11178668
Anti pULK1	Cell Signaling Technology	Cat# 14202; RRID:AB_2665508
Anti S6 Ribosomal Protein	Cell Signaling Technology	Cat# 2317; RRID:AB_2238583
Anti pS6 Ribosomal Protein	Cell Signaling Technology	Cat# 4858; RRID:AB_916156
Anti Cleaved caspase 3	Cell Signaling Technology	Cat# 9664; RRID:AB_2070042
Anti CD63	Abcam	Cat# ab108950; RRID:AB_10863101
Anti VAMP7	N/A	Clone TG158.2
Anti VAMP7	N/A	Rabbit serum TG50
Anti ATG5	Abcam	Cat# ab108327; RRID:AB_2650499
Anti p62	Abcam	Cat# ab101266; RRID:AB_10675814
Anti O-Linked N-Acetylglucosamine	Abcam	Cat# ab2739; RRID:AB_303264
Anti SNAP29	Synaptic Systems	Cat# 111 302; RRID:AB_887795
Anti Beta tubulin	N/A	Clone E7
Anti Tau1	Millipore	Cat# MAB3420; RRID:AB_11213630
Anti MAP2	Abcam	Cat# ab5392; RRID:AB_2138153
Anti Sec6	Stressgen / Enzo Life Sciences	Cat# sv021; RRID:AB_10618264
Anti GFP	Roche	Cat# 11814460001; RRID:AB_390913
Alexa Fluor 647 Phalloidin	Thermo Fisher Scientific	Cat# A22287; RRID:AB_2620155
Deposited Data		
Analyzed Proteomic Dataset from PC12	This paper	ProteomeXchange Consortium via PRIDE. ID: PXD020502 http://proteomecentral.proteomexchange.org/cgi/GetDataset?ID=PXD020502
Experimental Models: Cell lines		
PC12	ATCC	Cat# CRL-1721.1
Experimental Models: Organisms/Strains		
Rattus norvergicus	Janvier Labs (France)	Cat# RN-SD-F
Oligonucleotides		
Guide RNA to KO VAMP7 (sgRNA#5): GTGTGGAGGAAACTTCCTGG	This paper	N/A
Guide RNA to KO VAMP7 (sgRNA#3): AGTGGTTCCCCTGGCAACAA	This paper	N/A
Guide RNA to KO ATG5 (sgRNA#3): AAGAGTCAGCTATTTGACGC	This paper	N/A
Guide RNA to KO ATG5 (sgRNA#4): AAGAAGATGTTAGTGAGATT	This paper	N/A
Recombinant DNA		
GFP-VAMP7	Addgene	Cat# 42316
Nanobody mCherry-F1.1	This paper. Hybrigenics SA.	N/A
Chemicals		
Rapamycin	Sigma-Aldrich	Cat# 37094
Spautin	Sigma-Aldrich	Cat# SML0440
Bafilomycin A1	InvivoGen	Cat# TLRL-BAF1

(*Continued on next page*)

Continued

REAGENT or RESOURCE	SOURCE	IDENTIFIER
Torin1	InvivoGen	Cat# INH-TOR1
Software		
ImageJ	(Schneider et al., 2012)	https://imagej.nih.gov/ij
Icy	(de Chaumont et al., 2012)	http://icy.bioimageanalysis.org
R	N/A	https://www.r-project.org

RESOURCE AVAILABILITY

Lead Contact

Further information and requests for resources and reagents should be directed to and will be fulfilled by the Lead Contact, Thierry Galli (thierry.galli@inserm.fr).

Materials Availability

Plasmids and PC12 cell lines generated in this study have not been deposited to any public repository as they are easily generated. Should any of them be needed please inquiry with the lead contact. Previously published plasmids generated by the laboratory are available at Addgene.

No other unique reagent was generated in this study.

Data and Code Availability

The mass spectrometry proteomic data have been deposited at the ProteomeXchange Consortium via the PRIDE partner repository with the dataset identifier PXD020502.

EXPERIMENTAL MODEL AND SUBJECT DETAILS

Cell lines

PC12 cell lines (ATCC Cat# CRL-1721.1) were grown at 37°C and 5% CO_2 in RPMI supplemented with 10% Horse Serum (Thermo Fisher 26050088) and 5% Bovine Fetal Calf Serum (Biosera 017BS346). Plastic dishes were coated with a 1 mg/ml collagen (Sigma C7661) solution to obtain a collagen concentration of 1.83 $\mu g/cm^2$ on the culture dish. Induction of neurite-like extensions was triggered by incubating cells with differentiation media (RPMI + 1% Horse Serum + 50ng/ml NGF (Sigma-Aldrich)) for one week.

To prepare conditioned media we differentiated WT, VAMP7 KO and ATG5 KO PC12 cells in T150 flasks. The culture media was replaced on the 6th day of differentiation with fresh serum-free differentiation media (RPMI + 50ng/ml NGF) and left overnight. Media conditioned by WT, VAMP7 KO or ATG5 KO were collected (~20ml/dish), cell debris were cleared by 2,000 x g / 20min centrifugation, supplemented with 1% Horse serum and used to differentiate WT PC12 for one week. Culture media was replaced every 2 days.

After the treatment, cells were fixed and processed for immunocytochemistry. Neurites were visualized by tubulin staining.

Primary cultures

Primary neuronal cultures were prepared as previously described (Kaech and Banker, 2006). E18-E19 rat hippocampal and cortical neurons were dissected, enzymatically dissociated and plated onto poly-L-lysine coated glass coverslips (1 mg/ml) or plastic dishes (0.1 mg/ml) in MEM supplemented with 10% Horse serum and 0.6% Glucose. After 2 to 4 hours, the culture media was changed with neuronal N2 media. For confocal imaging analysis, hippocampal neurons were plated at a density of 9,000 neurons/cm^2 and for biochemical analysis, cortical neurons were plated at a density of 300,000 neurons/cm^2. No sex selection was performed during the extraction of the embryos.

Pregnant rats were terminally anesthetized with CO_2 before removing the embryos, no special ethical permission was required for this procedure. The embryos were decapitated immediately after removal from the uterus so no special ethical permission was required.

METHOD DETAILS

Cell treatments with chemicals

Rapamycin (Sigma-Aldrich, 37094), Spautin-1 (Sigma-Aldrich, SML0440), Torin1 (InvivoGen, INH-TOR1) and Bafilomycin A1 (InvivoGen, TLRL-BAF1) were diluted in culture media and added to either PC12 cells or primary neurons. To minimize cell stress during the treatments, we prepared 2X concentrated solutions and added them to the same amount of culture media in the culture dish. The concentrations and time of the treatments are detailed in the main text and figure legends.

Protein electrophoresis and western blot

Cells were extracted with a lysis buffer composed of Tris 50 mM; NaCl 150 mM; Triton X-100 1%; 3 mM EDTA and 1X complete protease inhibitor cocktail (Sigma Aldrich 05056489001). After extraction, samples were centrifuged at 12,000 × g at 4°C for 20 minutes and the supernatant was recovered. 20 – 30 μg of total protein was loaded into 12% Laemmli-SDS-PAGE gels and run at 80V for 30 minutes and then 110V for another 90 minutes approximately. Proteins were then transferred to a 0.2 μm nitrocellulose membrane at 400 mA for 2 – 3 hours at 4°C. Membranes were blocked with a Tris-based saline solution; 0,1% Tween-20 (TBST) and supplemented with 2,5% non-fat dry milk. Primary and secondary antibodies were incubated in TBST supplemented with 2.5% non-fat dry milk solution. Unless otherwise stated, all secondary antibodies were conjugated with Horse Radish Peroxidase. Membranes were developed with SuperSignal West Femto Maximum Sensitivity Substrate (Thermo Fisher 34095). 10 images over a 60 to 120 s time frame were acquired with a Chemidoc imager™ (BioRad). Non-saturated images were analyzed with Fiji/ImageJ to determine signal density. Unless otherwise stated, the signal of interest was expressed as a ratio to GAPDH to compensate for potential unequal sample loading.

Secretome fractionation

The day following cell seeding the complete culture media was changed with fresh control or treatment media and left overnight. Cells were processed for western blot as described. The cell culture media was recovered and centrifuged at 2,000 x g for 10 minutes to remove cell debris. The supernatant was then treated either with acetone and centrifuged at 16,000 x g to recover all proteins or centrifuged at 15,000 x g for 30 minutes to recover large EVs. The pellet was then re-suspended in lysis buffer with Triton-x100 at a final concentration of 1%. This was the 15K pellet. For WB analysis, 15μg of the cell lysate and 30% of the 15K pellets were loaded into a 12% pre-casted 4%–12% Bis-Tris gel (NuPAGE, Life Technologies) and then continued as a regular western blot analysis. All centrifugations were done at 4°C.

Lipidomic analysis

Lipids were extracted from cells using a modified version of the Bligh and Dyer's protocol. Lipidomic analyses were carried out as described previously on an Exion UPLC coupled with a SCIEX QTRAP 6500 PLUS system for polar lipids, and an Agilent 1260 HPLC coupled with a SCIEX QTRAP 5500 for neutral lipids (Song et al., 2020). All quantification experiments were conducted using internal standard calibration. In brief, polar lipids were separated on a Phenomenex Luna Silica 3 μm column (i.d. 150 × 2.0mm) under a binary gradient comprising mobile phase A (chloroform:methanol:ammonium hydroxide, 89.5:10:0.5) and mobile phase B (chloroform:methanol: ammonium hydroxide: water, 55:39:0.5:5.5) at a flow rate of 270μL/min and column oven temperature at 25°C. Individual polar lipid species were quantified by referencing to spiked internal standards of the same lipid class including PC-14:0/14:0, PE14:0/14:0, d_{31}-PS-16:0/18:1, PA-17:0/17:0, PG-14:0/14:0, C14:0-BMP, SM-d18:1/12:0, LPC-17:0, LPE-17:1, LPI-17:1, LPA-17:0, LPS-17:1, S1P-d17:1, Cer-d18:1/d_7-15:0, GluCer d18:1/8:0, GalCer d18:1/8:0 obtained from Avanti Polar Lipids (AL, USA) and PI-8:0/8:0 from Echelon Biosciences, Inc. (UT, USA). d_3-GM3 d18:1/18:0 and d_3-LacCer d18:1/16:0 were from Matreya LLC (PA, USA). Glycerol lipids including diacylglycerols (DAGs) and triacylglycerols (TAGs) were quantified using a modified version of reverse phase LC/MRM. Separation of neutral lipids were achieved on a Phenomenex Kinetex-C18 2.6 μm column (i.d. 4.6x100 mm) using an isocratic mobile phase containing chloroform:methanol:0.1 M ammonium acetate 100:100:4 (v/v/v) at a flow rate of 300 μL for 10 minutes. Levels of short-, medium-, and long-chain TAGs were calculated by referencing to spiked internal standards of TAG(14:0)$_3$-d_5, TAG(16:0)$_3$-d_5 and TAG(18:0)$_3$-d_5 obtained from CDN isotopes (Quebec, Canada), respectively. DAGs were quantified using d_5-DAG16:0/16:0 and d_5-DAG18:1/18:1 as internal standard from Avanti Polar Lipids. Free cholesterols and cholesteryl esters were analyzed as described previously with d_6-cholesterol and d_6-CE18:0 cholesteryl ester (CE) (CDN isotopes) as internal standards. Lipid levels in each sample were expressed in molar fractions normalized total polar lipids (sum of phospholipids and sphingolipids) for statistical analyses.

Proteomic analysis

Secretome purification

2ml of culture media were precipitated overnight at 4°C with TCA at 10% final v/v and centrifuged 20minutes at 20,000 x g. Pellets were washed 4 times with ethanol. After the last wash, the pellets were resuspended in 50μl of 5% SDS/100mM TEAB buffer, supplemented with 20mM TCEP and 50mM CAA for complete protein reduction and alkylation. Samples were incubated for 5minutes at 90°C and digested.

Reagents and chemicals

Dithiothreitol, iodoacetamide and ammonium bicarbonate were purchased from Sigma-Aldrich (St Louis, MO, USA), trifluoroacetic acid (TFA), formic acid, acetonitrile and HPLC-grade water were purchased from Fisher Scientific (Pittsburgh, PA, USA) at the highest purity grade.

Procedure

PC12 secretome and proteome were analyzed in three independent biological replicates, each analyzed in technical triplicates. Samples were digested following an S-Trap protocol using the S-Trap™ micro spin columns (Protifi, Huntington, NY, USA) either on 50 μg of total lysate proteins or proteins extracted from 2 mL of culture media. Briefly, samples were first supplemented with SDS to a final concentration of 5%. Proteins were reduced with 20mM TCEP and alkylated with 50mM CAA. Aqueous phosphoric acid was then

added to a final concentration of 1.2% followed by the addition of S-Trap binding buffer (90% aqueous methanol, 100mM TEAB, pH 7.1). The mixtures were loaded on the S-Trap columns. The columns were washed three times with 150μL S-Trap binding buffer. Samples were digested with 2μg of trypsin (Promega) at 47°C for 1h. After elution, peptides were vacuum dried and resuspended in 100μl 10% ACN, 0.1% TFA in HPLC-grade water prior to MS analysis. For each run, 1μL was injected in a nanoRSLC-Q Exactive PLUS (RSLC Ultimate 3000) (Thermo Scientific, Waltham MA, USA).

Peptides were loaded onto a μ-precolumn (Acclaim PepMap 100 C18, cartridge, 300μm i.d. × 5mm, 5μm, Thermo Scientific, MA, USA) and were separated on a 50 cm reversed-phase liquid chromatographic column (0.075mm ID, Acclaim PepMap 100, C18, 2μm, Thermo Scientific, MA, USA). Chromatography solvents were (A) 0.1% formic acid in water, and (B) 80% acetonitrile, 0.08% formic acid. Peptides were eluted from the column with the following gradient of 5% to 40% B for 120 minutes. One blank was run between each replicate to prevent sample carryover. Peptides eluting from the column were analyzed by data dependent MS/MS, using the top-10 acquisition method. Peptides were fragmented using higher-energy collisional dissociation (HCD). Briefly, the instrument settings were as follows: resolution was set to 70,000 for MS scans and 17,500 for the data dependent MS/MS scans in order to increase speed. The MS AGC target was set to 3.106 counts with maximum injection time set to 60 ms, while MS/MS AGC target was set to 1.105 with maximum injection time set to 60 ms. The MS scan range was from 400 to 2000 m/z. Dynamic exclusion was set to 30 s. The MS files were processed with the MaxQuant software version 1.6.6.0 and searched with Andromeda search engine against the UniProtKB/Swiss-Prot *Rattus Norvegicus* database (release 04-2019, 8036 entries). To search parent mass and fragment ions, we set an initial mass deviation of 4.5 ppm and 0.5 Da respectively. The minimum peptide length was set to 7 amino acids and strict specificity for trypsin cleavage was required, allowing up to two missed cleavage sites. Carbamidomethylation (Cys) was set as fixed modification, whereas oxidation (Met), N-term acetylation were set as variable. The match between runs option was enabled with a match time window of 0.7 minutes and an alignment time window of 20 minutes. The false discovery rates (FDRs) at the protein and peptide level were set to 1%. Scores were calculated in MaxQuant as described previously (Cox and Mann, 2008). For statistical analysis and graphical representations we used Perseus 1.6.7.0. For both proteome and secretome analysis we kept only proteins identified in all three biological replicates in at least one group (VAMP7 KO, ATG5 KO and/or WT). Missing values were imputed using width = 0.3 and down-shift = 1.8. For volcano plot we used t test, S0 = 2, FDR = 0.05. We annotated class of proteins according to GO, Keyword and Kegg databases. KFERQ motifs (CMA) were annotated according to a database obtained using scanprosite by scanning the rat proteome for the sequences [RK]-[IFVL]-[ED]-[RK]-Q and [IFVL]-[RK]-[RK]-[ED]-Q.

Immunofluorescence and microscopic imaging

Immunofluorescence

Cells were fixed with 4% para-formaldehyde and 4% sucrose for 20 minutes at room temperature. Cells were then permeabilized with 0.1% Triton X-100 for 6 minutes and then incubated for 30 minutes with a blocking solution consisting of 1% BSA and 0.1% Tween-20 in PBS. Primary antibodies were diluted in blocking solution and incubated for 90 minutes at room temperature. Secondary antibodies were conjugated with the fluorescent probes Alexa 488, 568, 594 or 647 and were diluted, along with DAPI, in 1% BSA/PBS and incubated for 60 minutes at room temperature. Coverslips were then mounted with in ProlongGold (Thermofisher) mounting media.

List of antibodies and dyes

Antibody	Catalog Number	WB dilution	IF dilution
Anti LC3B	Sigma-L7543	1/10000	1/500
Anti GAPDH	Sigma-G9545	1/40000	–
Anti ULK1	Cell Signaling-8054	1/2000	–
Anti pULK1	Cell Signaling-14202	1/2000	–
Anti S6 Ribosomal Protein	Cell Signaling-2317	1/2000	–
Anti pS6 Ribosomal Protein	Cell Signaling-4858	1/2000	–
Anti Cleaved caspase 3	Cell Signaling-9664	1/1000	–
Anti CD63	Abcam-ab108950	-	1/300
Anti VAMP7	Clone TG158.2	1/1000	1/200
Anti VAMP7	Clone TG50	1/1000	–
Anti ATG5	Abcam-ab108327	1/5000	–
Anti p62	Abcam-ab101266	1/5000	–
Anti O-Linked N-Acetylglucosamine	Abcam-ab2739	1/1000	–
Anti SNAP29	SySy-111 302	1/5000	1/1000
Anti Beta tubulin	Clone E7	–	1/8000

(*Continued on next page*)

Continued			
Antibody	Catalog Number	WB dilution	IF dilution
Anti Tau1	Millipore -MAB3420	–	1/2000
Anti MAP2	Abcam-ab5392	–	1/10000
Anti Sec6	Stressgen-vam sv021	1/1000	1/200
Anti GFP	Roche-11814460001	1/20000	1/100
Phalloidin	Life Technologies-A22287	–	1/1000

Confocal imaging

For high-magnification analysis, z stack confocal imaging was carried out on a TCS SP8 (93X, 1.3 NA, glycerol-immersion objective) microscope equipped with a supercontinuum fiber laser (WLL2). Pixel size as well as Z-step sizes were set to fulfill Nyquist criterion. In all cases, lasers and spectral bands were chosen to maximize signal recovery while avoiding signal bleed-through.

For the analysis of neurite length, low-magnification tile images (covering no less than 6mm^2) of hippocampal neurons or PC12 cells were acquired in a TCS SP8 microscope (20X, 0.75 NA, glycerol-immersion objective) or a Leica DMI6000B inverted microscope (HC PL Fluotar 20x/0.5) and then stitched using LAS X (Leica) or Grid/Collection stitching plugin from Fiji software respectively.

Neurons live imaging

2 DIV hippocampal neurons were transfected with mCherry-LC3B and GFP-VAMP7 or ATG9a-RFP and GFP-VAMP7 with the Lipofectamine 2000 reagent (Thermofisher) as described. Immediately after transfection, neurons were placed in control (DMSO) or treatment (Rapamycin 50nM) media. The following day, neurons were transferred to an imaging chamber (Chamlide EC-B18) and maintained in Krebs/Ringer buffer (140 mM NaCl, 2.5 mM KCl, 1.8 mM CaCl2, 1.0 mM MgCl2, 20 mM HEPES, 4.5g/ml glucose, and pH = 7.4) supplemented with insulin (500ng/ml), glucose 1mM and DMSO or Rapamycin according to the experimental procedure. The chamber was placed in a Leica DMI6000B inverted microscope with a 1.6X mag changer, a Leica 63X/1.4 NA Plan-Apochromat oil immersion objective and an ImagEMX2 EMCCD camera (Hamamatsu). Light sources used were a diode-pumped 25mW 561nm (Melles Griot) and a 200mW 488nm (Nichia) lasers, controlled by iLas2 targeted-laser illumination controller. Metamorph (Molecular Devices) software was used to control the acquisition and the microscopy system. The acquisition lasted for 1 minute acquiring 1 image every 200ms per channel.

CRISPR/Cas9 genetic engineering

To generate the Knock Out (KO) PC12 cell lines we used the RNA-guided Cas9 endonuclease system developed from the microbial clustered regularly interspaced short palindromic repeats (CRISPR) adaptive immune system (Ran et al., 2013). The guide RNAs sequences were chosen with the web-based selection tool CRISPOR which implements scoring algorithms based on their potential off-target and on-target DNA cleavage activity (Chari et al., 2017). The 2 highest-scored guide RNAs sequences were cloned into a pSpCas9(BB)-2A-GFP backbone plasmid. pSpCas9(BB)-2A-GFP (PX458) was a gift from Feng Zhang (Addgene plasmid #48138; http://addgene.org/48138; RRID: Addgene_48138). After confirmation of the correct insertion by colony PCR and sequencing, plasmids were amplified, purified and electroporated to PC12 cells with a bioRad electroporation device which allowed high number of electroporated cells with moderate plasmid expression. The following day, cells were trypsinized and detached from the culture dish, pelleted and re-suspended in PBS Ca^{2+}/Mg^{2+} free, EDTA 1mM, 25mM HEPES, 1% fetal bovine serum, penicillin and streptomycin. Cells were then sorted by a Fluorescence Activated Cell Sorter by placing one GFP-positive cell per wheel in a 96-multi well plate containing complete media supplemented with penicillin, streptomycin and kanamycin. Cells were amplified until final confirmation of gene knockout by protein electrophoresis and Western Blot.

List of guide RNA sequences

Target protein	Guide sequence	Target protein	Target cell
VAMP7 ***(sgRNA #5)***	GTGTGGAGGAAACTTCCTGG	VAMP7	PC12
VAMP7 (sgRNA #3)	AGTGGTTCCCCTGGCAACAA	VAMP7	PC12
ATG5 ***(sgRNA #3)***	AAGAGTCAGCTATTTGACGC	ATG5	PC12
ATG5 (sgRNA #4)	AAGAAGATGTTAGTGAGATT	ATG5	PC12

*Bold guide RNAs sequences were the most effective.

Selection of the VHHs against VAMP7

Recombinant GST-VAMP7 protein (Martinez-Arca et al., 2000) was biotinylated using EZ-Link Sulfo-NHS-Biotin (Thermo Fisher Scientific) using manufacturer conditions except for a two-fold molecular excess of Sulfo-NHS-Biotin. The unreacted Sulfo-NHS-Biotin

was eliminated using Prepacked Columns Sepadextran 25 Medium SC (Proteigene). Biotinylation and binding to the beads is checked by western blot using SA-HRP (Thermo Fisher Scientific). The Nali-H1 library of VHHs was screened against the recombinant biotinylated-VAMP7 as described previously (Moutel et al., 2016) after phage depletion using MBP-Ha-Gst-Flag recombinant protein. Biotinylated-VAMP7 protein was bound to Dynabeads M-280 Streptavidin (Invitrogen) at each round of selection, at a concentration gradually decreased: 100nM in first round, 50nM in second round and 10nM in third round. 1011 phages of the Nali-H1 library were used in the first round of selection. After the third round, 186 clones were randomly picked and tested in non-absorbed Phage ELISA assay using avidin-plates and biotinylated-VAMP7 Antigen (5μg/ml) for cross-validation (Matz and Chames, 2012). Anti-VAMP7 VHH F1.1 was recovered following this screen, then mCherry-tagged anti-VAMP7 VHH F1.1 were further validated by co-expression with GFP-tagged VAMP2, VAMP4, Sec22b as control and VAMP7.

Validation of F1.1 nanobody

VAMP7 and VAMP4 in pB27 (LexA-Bait), VAMP4 and Sec22 in pB29 (Bait-LexA) were transformed in L40ΔGal4 (mata). Preys: F1-1 pP9 (Gal4AD-F1-1) or pP9 empty vector were transformed in YHGX13 (Y187 ade2-101::loxP-kanMX-loxP, mata). After mating in 96 well plate, growth was tested in drop out minus Leu and Trp (Non-Selective) and on drop out minus Leu, Trp and His to check the interaction and confirm the non-auto-activation with the empty plasmid.

QUANTIFICATION AND STATISTICAL ANALYSIS

Image analysis

Neurite length

Low-magnification tile images (covering no less than 6mm^2) of hippocampal neurons or PC12 cells were analyzed with the Simple Neurite Tracer plugin (Longair et al., 2011) in Fiji/ImageJ. The length of all processes was quantified for all cells present in the image.

In neurons the axons were defined as any process longer than 100μm and Tau1-positive. Multi-polar neurons are those that have two or more axons. The total axonal length is the cumulative lengths of the longest and smaller branches of the axon.

In PC12 cells, we determined the length of the longest, uninterrupted process of every cell, and the cumulative length of the branches emerging from this process.

Spots detection and co-localization analysis

Stacked confocal images were analyzed with the "spot detector" (Olivo-Marin, 2002) and "co-localization studio" plugins in Icy software (de Chaumont et al., 2012). Spots were detected by first processing the original images to obtain coefficient images to remove background and noise. Then a wavelet adaptive threshold is computed using always a combination of scale 2 and scale 3 and threshold between 30 and 80 to define the size of the spots and sensitivity of the algorithms respectively. Co-localization was performed with the object-based method by first segmenting the signal of interest (spot detector plugin) and then analyzing their spatial distributions with second-order statistics (Lagache et al., 2015). Statistically significative (p value < 0.05) co-localizing spots were used to calculate the average proportion of co-localization under each experimental condition.

For CD63 and RTN3 structures, binary masks were generated from object segmentation with the spot detector icy plugin. The volume overlap between CD63 and RTN3 structures was determined using 3D roi manager plugin (Ollion et al., 2013) under FiJi (Schindelin et al., 2012). Co-localization was considered when the volume overlap was at least 90%.

Vesicle track detection and analysis

Time-lapse images were first segmented with the "spot detector" plug-in in icy software to detect vesicles in the distal axon of hippocampal neurons. Trajectories were then estimated using the "Spot tracking" plug-in in icy software (Chenouard et al., 2013). Trajectories were extracted using a probabilistic tracking method which at any given time point considers multiple past and futures frames for building the best set of tracks. The set of parameters used were the ones automatically determined by the plug-in.

Statistical analysis

Unless otherwise stated all statistical analysis was performed with the R software. When pooling data from different replicate experiments, the data was standardized as follows: "std value (x) = (x – sample mean)/sample standard deviation." When the experimental design required a single pairwise comparison, Student t tests were applied. If the experimental design required the comparison of multiple conditions with a single control condition an ANOVA with orthogonal contrasts was applied. In the cases where we needed to do multiple comparisons, we applied an ANOVA test followed by a Tukey's HSD test.

The exact value of n, what it represents and center and dispersion measures are described in the figures and figure legends. In experiments where we measured neurite length, each cell was considered as an independent statistical observation. Statistical observations come from three independent experiments. Significance was defined as a p value lower than 0.05 unless otherwise stated. The exact p value is written in the figures.

The lower and upper hinges of all boxplots correspond to the first and third quartiles respectively (the 25th and 75th percentiles). The upper whisker extends from the hinge to the largest value no further than 1.5 * IQR from the hinge (where IQR is the inter-quartile range, or distance between the first and third quartiles). The lower whisker extends from the hinge to the smallest value at most 1.5 * IQR of the hinge. Data beyond the end of the whiskers are called "outlying" points and are plotted individually.